Estimates of Lightning NO$_x$ Production based on High Resolution OMI NO$_2$ Retrievals over the Continental US

Xin Zhang[1,2], Yan Yin[1,2], Ronald van der A[2,3], Jeff L. Lapierre[4], Qian Chen[1,2], Xiang Kuang[1,2], Shuqi Yan[2], Jinghua Chen[1,2], Chuan He[1,2], and Rulin Shi[1,2]

[1] Collaborative Innovation Center on Forecast and Evaluation of Meteorological Disasters/Key Laboratory for Aerosol-Cloud-Precipitation of China Meteorological Administration, Nanjing University of Information Science and Technology (NUIST), Nanjing 210044, China
[2] Department of Atmospheric Physics, Nanjing University of Information Science and Technology (NUIST), Nanjing 210044, China
[3] Royal Netherlands Meteorological Institute (KNMI), Department of Satellite Observations, De Bilt, the Netherlands
[4] Earth Networks, Germantown, Maryland, USA

Correspondence: Yan Yin (yinyan@nuist.edu.cn)

Abstract. Lightning serves as the dominant source of nitrogen oxides (NO$_x$ = NO + NO$_2$) in the upper troposphere (UT), with strong impact on ozone chemistry and the hydroxyl radical production. However, the production efficiency (PE) of lightning nitrogen oxides (LNO$_x$) is still quite uncertain (32 – 1100 mol NO per flash). Satellite measurements are a powerful tool to estimate LNO$_x$ directly as compared to conventional platforms. To apply satellite data in both clean and polluted regions, a new algorithm for calculating LNO$_x$ has been developed that uses the Berkeley High Resolution (BEHR) v3.0B NO$_2$ product and the Weather Research and Forecasting-Chemistry (WRF-Chem) model. LNO$_x$ PE over the continental US is estimated using the NO$_2$ product of the Ozone Monitoring Instrument (OMI) satellite and the Earth Networks Total Lightning Network (ENTLN) data. Focusing on the summer season during 2014, we find that the lightning NO$_2$ (LNO$_2$) PE is 32 $\pm$ 15 mol NO$_2$ flash^{-1} and 6 $\pm$ 3 mol NO$_2$ stroke^{-1} while LNO$_x$ PE is 90 $\pm$ 49 mol NO$_x$ flash^{-1} and 17 $\pm$ 9 mol NO$_x$ stroke^{-1}. Results reveal that our method reduces sensitivity to the background NO$_2$ and includes much of the below-cloud LNO$_2$. As the LNO$_x$ parameterization varies in studies, the sensitivity of our calculations to the setting of the amount of lightning NO (LNO) is evaluated. Careful consideration of the ratio of LNO$_2$ to NO$_2$ is also needed, given its large influence on the estimation of LNO$_2$ PE.

1 Introduction

Nitrogen oxides (NO$_x$) near the Earth's surface are mainly produced by soil, biomass burning and fossil fuel combustion, while NO$_x$ in the middle and upper troposphere originates largely from lightning and aircraft emissions. NO$_x$ plays an important role in the production of ozone (O$_3$) and the hydroxyl radical (OH). While the anthropogenic sources of NO$_x$ are largely known, lightning nitrogen oxides (LNO$_x$) are still the source with the greatest uncertainty, though they are estimated to range between 2 and 8 Tg N yr^{-1} (Schumann and Huntrieser, 2007). LNO$_x$ is produced in the upper troposphere (UT) by O$_2$ and N$_2$ dissociation in the hot lightning channel as described by the Zel'dovich mechanism (Zel'dovich and Raizer, 1967). With the recent updates

1

of UT NO_x chemistry, the day time lifetime of UT NO_x is evaluated to be ~ 3 h near thunderstorms and $\sim 0.5 - 1.5$ days away from thunderstorms (Nault et al., 2016, 2017). This results in enhanced O_3 production in the cloud outflow of active convection (Pickering et al., 1996; Hauglustaine et al., 2001; DeCaria et al., 2005; Ott et al., 2007; Dobber et al., 2008; Allen et al., 2010; Finney et al., 2016). As O_3 is known as a greenhouse gas, strong oxidant and absorber of ultraviolet radiation (Myhre et al., 2013), the contributions of LNO_x to O_3 production also have an effect on climate forcing. Finney et al. (2018) found different impacts on atmospheric composition and radiative forcing when simulating future lightning using a new upward cloud ice flux (IFLUX) method versus the commonly used cloud-top height (CTH) approach. While lightning is predicted to increase by 5 — 16% over the next century with the CTH approach (Clark et al., 2017; Banerjee et al., 2014; Krause et al., 2014), a 15% decrease in lightning was estimated with IFLUX in 2100 under a strong global warming scenario (Finney et al., 2018). As a result of the different effects on radiative forcing from ozone and methane, a net positive radiative forcing was found with the CTH approach while there is little net radiative forcing with the IFLUX approach (Finney et al., 2018). However, the convective available potential energy (CAPE) times the precipitation rate (P) proxy predicts a $12 \pm 5\%$ increase in the Continental US (CONUS) lightning strike rate per kelvin of global warming (Romps et al., 2014), while the IFLUX proxy predicts the lightning will only increase 3.4%/K over the CONUS. Recently, Romps (2019) compared the CAPE $\times$ P proxy and IFLUX method in cloud-resolving models. They report that higher CAPE and updraft velocities caused by global warming could lead to the large increases in tropical lightning simulated by CAPE $\times$ P proxy, while IFLUX proxy predicts little change in tropical lightning because of the small changes in water mass fluxes.

In the view of the region dependent lifetime of NO_x and the difficulty of measuring LNO_x directly, a better understanding of the LNO_x production is required, especially in the tropical and mid-latitude regions in summer. Using its distinct spectral absorption lines in the near-ultraviolet (UV) and visible (VIS) range (Platt and Perner, 1983), NO_2 can be measured by satellite instruments like the Global Ozone Monitoring Experiment (GOME; Burrows et al., 1999; Richter et al., 2005), Scanning Imaging Absorption Spectrometer for Atmospheric Chartography (SCIAMACHY; Bovensmann et al., 1999), the Second Global Ozone Monitoring Experiment (GOME-2; Callies et al., 2000) and the Ozone Monitoring Instrument (OMI; Levelt et al., 2006). OMI has the highest spatial resolution, least instrument degradation and longest record among these satellites (Krotkov et al., 2017). Satellite measurements of NO_2 are a powerful tool compared to conventional platforms, because of its global coverage, constant instrument features and temporal continuity.

Recent studies have determined and quantified LNO_x using satellite observations. Beirle et al. (2004) constrained the LNO_x production to 2.8 (0.8 – 14) Tg N yr^{-1} by combining GOME NO_2 data and flash counts from the Lightning Imaging Sensor (LIS) aboard the Tropical Rainfall Measurement Mission (TRMM) over Australia. Boersma et al. (2005) estimated the global LNO_x production of 1.1 – 6.4 Tg N yr^{-1} by comparing GOME NO_2 with distributions of LNO_2 modeled by Tracer Model 3 (TM3). Martin et al. (2007) analyzed SCIAMACHY NO_2 columns with Goddard Earth Observing System chemistry model (GEOS-Chem) simulations to identify LNO_x production amounting to 6 ± 2 Tg N yr^{-1}.

As these methods focus on monthly or yearly mean NO_2 column densities, more recent studies applied specific approaches to investigate LNO_x directly over active convection. Beirle et al. (2006) estimated LNO_x as 1.7 (0.6 – 4.7) Tg N yr^{-1} based on a convective system over the Gulf of Mexico, using National Lightning Detection Network (NLDN) observations and

GOME NO_2 column densities. However, this study assumed that all the enhanced NO_2 originated from lightning and did not consider the contribution of anthropogenic emissions. Beirle et al. (2010) analyzed LNO_x production systematically using the global dataset of SCIAMACHY NO_2 observations combined with flash data from the World Wide Lightning Location Network (WWLLN). Their analysis was restricted to 30×60 km^2 satellite pixels where the flash rate exceeded 1 flash km^{-2} hr^{-1}. But they found LNO_x production to be highly variable and correlations between flash rate densities and LNO_x production are low in some cases. Bucsela et al. (2010) estimate LNO_x production as $\sim 100 - 250$ mol NO_x/flash for four cases, using the DC-8 and OMI data during NASA's Tropical Composition, Cloud and Climate Coupling Experiment (TC^4).

Based on the approach used by Bucsela et al. (2010), a special algorithm was developed by Pickering et al. (2016) to retrieve LNO_x from OMI and the WWLLN. The algorithm takes the OMI tropospheric slant column density (SCD) of NO_2 (S_{NO_2}) as the tropospheric slant column density of LNO_2 (S_{LNO_2}) by using cloud radiance fraction (CRF) greater than 0.9 to minimize or screen the lower tropospheric background. To convert the S_{LNO_2} to the tropospheric vertical density (VCD) of LNO_x (V_{LNO_x}), an air mass factor (AMF) is calculated by dividing the a priori S_{LNO_2} by the a priori V_{LNO_x}. Since they considered NO_2 above the cloud as LNO_2 in the algorithm due to the difficulty and uncertainty in determining the background NO_2, their AMF and derived VCD of LNO_x (LNO_2) is named as $AMF_{LNO_x Clean}$ ($AMF_{LNO_2 Clean}$) and $LNO_x Clean$ ($LNO_2 Clean$), respectively. Unless otherwise specified, abbreviations S and V are respectively defined as the tropospheric SCD and VCD in this paper. The a priori S_{LNO_2} is calculated using a radiative transfer model and a profile of LNO_2 simulated by the NASA Global Modeling Initiative (GMI) chemical transport model. The a priori V_{LNO_x} is also obtained from the GMI model. Results for the Gulf of Mexico during $2007 - 2011$ summer yield LNO_x production of 80 ± 45 mol NO_x per flash. Among several substantial sources of uncertainty, significant uncertainty exists in characterizing background NO_x ($3\% \sim >30\%$) in this region (Pickering et al., 2016).

More recently Bucsela et al. (2019) obtained an average production efficiency (PE) of 180 ± 100 mol per flash over East Asia, Europe and North America based on a modification of the method used in Pickering et al. (2016). A power function between LNO_x and lightning flash rate was established, while the minimum flash-rate threshold was not applied. The tropospheric NO_x background was removed by subtracting temporal average of NO_x at each box where the value was weighted by the number of OMI pixels which meet the optical cloud pressure and CRF criteria required to be considered deep convection but has 1 flash or less instead. The lofted pollution was considered as 15% of total NO_x according to the estimation from DeCaria et al. (2000, 2005) and the average chemical delay was adjusted by 15% following the 3-hour LNO_x lifetime in the nearby field of convection (Nault et al., 2017). However, there were negative LNO_x values caused by the overestimation of the tropospheric background and stratospheric NO_2 at some locations.

On the other hand, Lapierre et al. (2019) constrained LNO_2 to 1.1 ± 0.6 mol NO_2/stroke for intracloud (IC) strokes and 10.0 ± 4.9 mol NO_2/stroke for cloud-to-ground (CG) strokes over the CONUS. LNO_2 per stroke was scaled to 54.4 mol NO_x/flash using mean values of strokes per flash and the ratio of NO to NO_2 in the UT. They used the regridded Berkeley High-Resolution (BEHR) V3.0A $0.05° \times 0.05°$ "visible only" NO_2 VCD (V_{vis}) product which includes two parts of NO_2 that can be "seen" by the satellite. The first part is the NO_2 above clouds (pixels with CRF > 0.9) and the second part is the NO_2 detected from cloud free areas. A threshold of 3×10^{15} molecules cm^{-2}, the typical urban NO_2 concentration, was applied to mask the

contaminated grid cells (Beirle et al., 2010; Laughner and Cohen, 2017). The main difference between Lapierre et al. (2019) and Pickering et al. (2016) is the air mass factor for lightning (AMF_{LNO_x}) implemented in the basic algorithm. In Lapierre et al. (2019), the air mass factor was used to convert S_{NO_2} to V_{vis}, while in Pickering et al. (2016) it was used to convert S_{LNO_2} to V_{LNO_x}, assuming that all S_{NO_2} is generated by lightning.

95   To apply the approach used by Bucsela et al. (2010), Pickering et al. (2016), Bucsela et al. (2019) and Lapierre et al. (2019) without geographic restrictions, contamination by anthropogenic emissions must be taken into account in detail. The Weather Research and Forecasting (WRF) model coupled with chemistry (WRF-Chem) has been employed to evaluate the convective transport and chemistry in many studies (Barth et al., 2012; Wong et al., 2013; Fried et al., 2016; Li et al., 2017). Meanwhile, Laughner and Cohen (2017) showed that the OMI AMF is increased by ~35% for summertime when LNO_2 simulated by WRF-

100 Chem is included in the a priori profiles to match aircraft observations. The simulation agrees with observed NO_2 profiles and the bias of AMF related to these observations is reduced to $< \pm 4\%$ for OMI viewing geometries.

In this paper, we focus on the estimation of LNO_2 production per flash (LNO_2/flash), LNO_x production per flash (LNO_x/flash), LNO_2 production per stroke (LNO_2/stroke) and LNO_x production per stroke (LNO_x/stroke) in May–August (MJJA) 2014 by developing an algorithm similar to Pickering et al. (2016) based on the BEHR NO_2 retrieval algorithm (Laughner et al., 2018a,

105 b), but it performs better over background NO_2 sources. Section 2 describes the satellite, lightning data, model settings and the algorithm in detail. Section 3 explores the suitable data criteria, compares different methods and evaluates the effect of cloud and LNO_x parameterization on LNO_x production estimation. Section 4 examines the effect of different sources of the uncertainty on the results. Conclusions are summarized in Section 5.

2   Data and Methods

110 ### 2.1   Ozone Monitoring Instrument (OMI)

OMI is carried on the Aura satellite (launched in 2004), a member of A-train satellite group (Levelt et al., 2006, 2018). OMI passes over the equator at $\sim$ 13:45 LT (ascending node) and has a swath width of 2600 km, with a nadir field-of-view resolution of $13 \times 24 \, km^2$. Since the beginning of 2007, some of the measurements have become useless as a result of anomalous radiances called the "row anomaly" (Dobber et al., 2008; KNMI, 2012). For the current study, we used the NASA standard product V3.0

115 (Krotkov et al., 2017) as input to the LNO_x retrieval algorithm.

The main steps of calculating the NO_2 tropospheric VCD (V_{NO_2}) in the NASA product include:

1. SCDs are determined by the OMI-optimized differential optical absorption spectroscopy (DOAS) spectral fit;

2. A corrected ("de-striped") SCD is obtained by subtracting the cross-track bias caused by an instrument artifact from the measured slant column;

120 3. The AMF for stratospheric (AMF_{strat}) or tropospheric column (AMF_{trop}) is calculated from the NO_2 profile integrated vertically using weighted scattering weights with the a priori profiles. These profiles are obtained from GMI monthly mean profiles using four years (2004 – 2007) simulation;

4. The stratospheric NO_2 VCD (V_{strat}) is calculated from the subtraction of a priori contribution from tropospheric NO_2 and a three-step (interpolation, filtering, and smoothing) algorithm (Bucsela et al., 2013);

125   5. V_{strat} is converted to the slant column using AMF_{strat} and subtracted from the measured SCDs to yield S_{NO_2}, leading to $V_{NO_2} = S_{NO_2}/AMF_{trop}$.

Based on this method, we developed a new AMF_{LNO_x} to obtain the desired V_{LNO_x} ($V_{LNO_x} = S_{NO_2}/AMF_{LNO_x}$) to replace the original step 5. Details of this algorithm are discussed in section 2.4.

2.2   The Earth Networks Total Lightning Detection Network (ENTLN)

130   The Earth Networks Total Lightning Network (ENTLN) operates a system of over 1500 ground-based stations around the world with more than 900 sensors installed in the CONUS (Zhu et al., 2017). Both IC and CG lightning flashes are located by the sensors with detection frequency ranging from 1 Hz to 12 MHz based on the electric field pulse polarity and wave shapes. Groups of pulses are classified as a flash if they are within 700 ms and 10 km. In the preprocessed data obtained from the ENTLN, both strokes and lightning flashes composed of one or more strokes are included.

135   Rudlosky (2015) compared ENTLN combined events (IC and CG) with LIS flashes and found that the relative flash detection efficiency of ENTLN over CONUS increases from 62.4% during 2011 to 79.7% during 2013. Lapierre et al. (2019) also compared combined ENTLN and the NLDN dataset with data from the LIS during 2014 and found the detection efficiencies of IC flashes and strokes to be 88% and 45%, respectively. Since we only use the ENTLN data in 2014 as Lapierre et al. (2019) and NLDN detection efficiency of IC pulses should be lower than 33% which is calculated by the data in 2016 (Zhu et al.,
140   2016), only the IC flashes and strokes are divided by 0.88 and 0.45, respectively, while CG flashes and strokes are unchanged because of the high detection efficiency.

2.3   Model Description

The present study uses WRF-Chem version 3.5.1 (Grell et al., 2005) with a horizontal grid size of 12×12 km^2 and 29 vertical levels (Fig. 1). The initial and boundary conditions of meteorological parameters are provided by the North American
145   Regional Reanalysis (NARR) dataset with a 3 hourly time resolution. Based on Laughner et al. (2018b), 3D wind fields, temperature and water vapor are nudged towards the NARR data. Outputs from the version 4 of Model for Ozone and Related chemical Tracers (MOZART-4; Emmons et al., 2010) were used to generate the initial and boundary conditions of chemical species. Anthropogenic emissions are driven by the 2011 National Emissions Inventory (NEI), scaled to model years by the Environmental Protection Agency annual total emissions (EPA and OAR, 2015). The Model of Emissions of Gases and Aerosol
150   from Nature (MEGAN; Guenther et al., 2006) is used for biogenic emissions. The chemical mechanism is the version 2 of Regional Atmospheric Chemistry Mechanism (RACM2; Goliff et al., 2013) with updates from Browne et al. (2014) and Schwantes et al. (2015). In addition, lightning flash rate based on the level of neutral buoyancy parameterization (Price and Rind, 1992) and LNO_x parameterizations are activated (200 mol NO flash^{-1}, the factor to adjust the predicted number of flashes is set to 1; hereinafter referred to as "1×200 mol NO flash^{-1}"). Although the simulated total flash densities are higher
155   in the Southeast US and lower in the North Central US (Fig. 2), the criteria in Sect. 3.1 could limit this effect on the estimation

of LNO$_x$ production and Sect. 3.4 will use another simulation to test this problem. The bimodal profile modified from the standard Ott et al. (2010) profile (Laughner and Cohen, 2017) is employed as the vertical distribution of lightning NO (LNO) in WRF-Chem, while LNO and LNO$_2$ profiles are defined as the difference of vertical profiles between simulations with and without lightning.

2.4 Method for Deriving AMF

The V$_{\mathrm{LNO}_x}$ near convection is calculated according:

$$V_{\mathrm{LNO}_x} = \frac{S_{\mathrm{NO}_2}}{AMF_{\mathrm{LNO}_x}} \tag{1}$$

where S_{NO_2} is the OMI-measured tropospheric slant column NO$_2$ and AMF$_{\mathrm{LNO}_x}$ is a customized lightning air mass factor. The concept of AMF$_{\mathrm{LNO}_x}$ was also used in Beirle et al. (2009) to investigate the sensitivity of satellite instruments for freshly produced lightning NO$_x$. In order to estimate LNO$_x$, we define the AMF$_{\mathrm{LNO}_x}$ as the ratio of the "visible" modeled NO$_2$ slant column to the total modeled tropospheric LNO$_x$ vertical column (derived from the a priori NO and NO$_2$ profiles, scattering weights, and radiance cloud fraction):

$$AMF_{\mathrm{LNO}_x} = \frac{(1-f_r) \int_{p_{surf}}^{p_{tp}} w_{clear}(p) NO_2(p)\, dp + f_r \int_{p_{cloud}}^{p_{tp}} w_{cloudy}(p) NO_2(p)\, dp}{\int_{p_{surf}}^{p_{tp}} LNO_x(p)\, dp} \tag{2}$$

where f_r is the radiance cloud fraction, p_{surf} is the surface pressure, p_{tp} is the tropopause pressure, p_{cloud} is the cloud optical pressure (CP), w_{clear} and w_{cloudy} are respectively the pressure dependent scattering weights from the TOMRAD lookup table (Bucsela et al., 2013) for clear and cloudy parts, and $NO_2(p)$ is the modeled NO$_2$ vertical profile. Details of these standard parameters and calculation methods are given in Laughner et al. (2018a). $LNO_x(p)$ is the LNO$_x$ vertical profile calculated by the difference of vertical profiles between WRF-Chem simulations with and without lightning.

Please note that the CP is a reflectance-weighted pressure retrieved by the collision-induced O$_2$-O$_2$ absorption band near 477 nm (Acarreta et al., 2004; Sneep et al., 2008; Stammes et al., 2008). For a deep convective cloud with lightning, the CP lies below the geometrical cloud top which is much closer to that detected by thermal infrared sensors, such as the CloudSat and the Aqua MODerate-resolution Imaging Spectrometer (MODIS) (Vasilkov et al., 2008; Joiner et al., 2012). Hence, the tropospheric NO$_2$ measured by OMI lies inside the cloud rather than above the cloud top. In the following, "above cloud" or "below cloud" is relative to the cloud pressure detected by OMI. The sensitivity study of Beirle et al. (2009) compared the chemical compositions from the cloud bottom to the cloud top and revealed that a significant fraction the NO$_2$ within the cloud originating from lightning can be detected by the satellite. This valuable cloud pressure concept has been applied not only in the LNO$_x$ research but also in the cloud slicing method of deriving the UT O$_3$ and NO$_x$ (Ziemke et al., 2009; Choi et al., 2014; Strode et al., 2017; Ziemke et al., 2017; Marais et al., 2018). As discussed in Pickering et al. (2016), the ratio of V$_{\mathrm{LNO}_2}$ seen by OMI to V$_{\mathrm{LNO}_x}$ is partly influenced by p_{cloud}. The effects of LNO$_2$ below the cloud will be discussed in Sect. 3.4.

To compare our results with those of Pickering et al. (2016) and Lapierre et al. (2019), we calculate their $AMF_{LNO_x\,Clean}$ and $AMF_{NO_2\,Vis}$ respectively:

$$AMF_{LNO_x\,Clean} = \frac{(1-f_r)\int_{p_{surf}}^{p_{tp}} w_{clear}(p)LNO_2(p)\,dp + f_r\int_{p_{cloud}}^{p_{tp}} w_{cloudy}(p)LNO_2(p)\,dp}{\int_{p_{surf}}^{p_{tp}} LNO_x(p)\,dp} \tag{3}$$

$$AMF_{NO_2\,Vis} = \frac{(1-f_r)\int_{p_{surf}}^{p_{tp}} w_{clear}(p)NO_2(p)\,dp + f_r\int_{p_{cloud}}^{p_{tp}} w_{cloudy}(p)NO_2(p)\,dp}{(1-f_g)\int_{p_{surf}}^{p_{tp}} NO_2(p)\,dp + f_g\int_{p_{cloud}}^{p_{tp}} NO_2(p)\,dp} \tag{4}$$

where f_g is the geometric cloud fraction and $LNO_2(p)$ is the modeled LNO_2 vertical profile. Besides these AMFs, another AMF called $AMF_{LNO_2\,Vis}$ is developed for comparison later.

$$AMF_{LNO_2\,Vis} = \frac{(1-f_r)\int_{p_{surf}}^{p_{tp}} w_{clear}(p)NO_2(p)\,dp + f_r\int_{p_{cloud}}^{p_{tp}} w_{cloudy}(p)NO_2(p)\,dp}{(1-f_g)\int_{p_{surf}}^{p_{tp}} LNO_2(p)\,dp + f_g\int_{p_{cloud}}^{p_{tp}} LNO_2(p)\,dp} \tag{5}$$

A full list of definitions of the used AMFs is shown in Appendix A.

2.5 Procedures for Deriving LNO$_x$

V_{LNO_x} is re-gridded to $0.05° \times 0.05°$ grids using the constant value method (Kuhlmann et al., 2014). Then, it is analyzed in $1° \times 1°$ grid boxes with a minimum of fifty valid $0.05° \times 0.05°$ grids to minimize the noise. The minimum value is between five satellite pixels in Pickering et al. (2016) and three satellite pixels in Bucsela et al. (2019) or Allen et al. (2019). The main procedures used to derive LNO$_x$ are as follows:

CRFs (CRFs $\geq$ 70%, CRFs $\geq$ 90% and CRFs = 100%) and CP $\leq$ 650 hPa are various criteria of deep convective clouds for OMI pixels (Ziemke et al., 2009; Choi et al., 2014; Pickering et al., 2016). The effect of different CRFs on the retrieved LNO$_x$ is explored in section 3.2. Furthermore, another criterion of cloud fractions (CFs) is applied to the WRF-Chem results for the successful simulation of convection. The CFs are defined as the maximum cloud fraction calculated by the Xu-Randall method between 350 and 400 hPa (Xu and Randall, 1996; Strode et al., 2017). This atmospheric layer (between 350 and 400 hPa) avoids any biases in the simulation of high clouds. We choose CFs $\geq$ 40% suggested by Strode et al. (2017) to determine cloudy or clear for each simulation grid.

Besides cloud properties, a time period and sufficient flashes (or strokes) are required for fresh LNO$_x$ to be detected by OMI. The time window (t_{window}) is the hours prior to the OMI overpass time. t_{window} is limited to 2.4 h by the mean wind speed at pressure levels 500 – 100 hPa during OMI overpass time and the square root of the $1° \times 1°$ box over the CONUS (Lapierre et al., 2019). Meanwhile, 2400 flashes box^{-1} and 8160 strokes box^{-1} per 2.4 hour time window are chosen as sufficient for detecting LNO$_x$ (Lapierre et al., 2019). These criteria will result in a low bias in the PE results, as Bucsela et al. (2019) found that the PE is larger at small flash rates which are discarded here.

To ensure that lightning flashes are simulated successfully by WRF-Chem, the threshold of simulated total lightning flashes (TL) per box is set to 1000, which is fewer than that used by the ENTLN lightning observation, considering the uncertainty of lightning parameterization. In view of other NO$_2$ sources in addition to LNO$_2$, the ratio of modeled lightning NO$_2$ above cloud

215　(LNO$_2$Vis) to modeled NO$_2$ above cloud (NO$_2$Vis) is defined to check whether enough LNO$_2$ can be detected by OMI. The ratio $\geq$ 50% indicates that more than half of the NO$_x$ above the cloud must have a LNO$_x$ source.

Finally, the NO$_2$ lifetime against oxidation should be taken into account. As estimated by Nault et al. (2016), the lifetime (τ) of NO$_2$ in the near field of convections is $\sim$ 3 h. The initial value of NO$_2$ is solved by Eq. 6 as

$$NO_2(0) = NO_2(OMI) \times e^{0.5t/\tau} \tag{6}$$

220　where $NO_2(0)$ is the moles of NO$_2$ emitted at time t = 0, $NO_2(OMI)$ is the moles of NO$_2$ measured at the OMI overpass time and $0.5t$ is the half cross grid time which is 1.2 h, assuming that lightning occurred at the center of each 1° $\times$ 1° box. For each grid box, the mean LNO$_x$ vertical column is obtained by averaging V$_{\text{LNO}_x}$ values from all regridded 0.05° $\times$ 0.05° pixels in the box. This mean value is converted to moles LNO$_x$ using the dimensions of the grid box. Two methods are applied to estimate the seasonal mean LNO$_2$/flash, LNO$_x$/flash, LNO$_2$/stroke and LNO$_x$/stroke:

225　(1) summation method: dividing the sum of LNO$_x$ by the sum of flashes (or strokes) in each 1° $\times$ 1° box in MJJA 2014;

(2) linear regression method: applying the linear regression to daily mean values of LNO$_x$ and flashes (or strokes).

3　Results

3.1　Criteria Determination

To determine the suitable criteria from conditions defined in section 2.5, six different combinations are defined (Table 1) and
230　applied to the original data with a linear regression method (Table 2).

A daily search of the NO$_2$ product for coincident ENTLN flash (stroke) data results in 99 (102) valid days under the CRF90_ENTLN condition. Taking the flashes type ENTLN data as an example, the number of valid days decreases from 99 to 81 under the CRF90_ENTLN_TL1000_ratio50 condition, while LNO$_x$/flash increases from 52.1 $\pm$ 51.1 mol/flash to 54.5 $\pm$ 48.1 mol/flash. The result is almost the same as that under the CRF90_ENTLN_TL1000 condition which is without the
235　condition of ratio $\geq$ 50%. Although this indicates the criterion of TL works well, it is better to include the ratio in case of some exceptions in the different AMF methods. Since CF $\geq$ 40% leads to a sharp loss of valid numbers and production, therefore, it is not a suitable criterion. Instead the CRF criteria are used. Finally, coincident ENTLN data, TL $\geq$ 1000 and ratio $\geq$ 50% are chosen as the thresholds to explore the effects of three different CRF conditions (CRF $\geq$ 70%, CRF $\geq$ 90% and CRF = 100%) on LNO$_x$ production (Table 3).

240　Apart from the fewer valid days under higher CRF conditions (CRF $\geq$ 90% and CRF = 100%), LNO$_x$/flash increases from 35.7 $\pm$ 36.8 mol/flash to 54.5 $\pm$ 48.1 mol/flash and decreases again to 20.8 $\pm$ 37.4 mol/flash while LNO$_x$/stroke enhances from 4.1 $\pm$ 3.9 mol/stroke to 7.0 $\pm$ 4.8 mol/stroke and drops again to 2.6 $\pm$ 4.0 mol/stroke (Table 3), as the CRF criterion increases from 70% to 90% and to 100%. The increment of LNO$_x$ PE caused by the CRF increase from 70% to 90% is opposite to the result of Pickering et al. (2016). This is an effect of the consideration of NO$_2$ contamination transported from the boundary
245　layer in our method. Although enhanced NO$_x$ is often observed in regions with CRF > 70% (Pickering et al., 2016), the

following analysis will be based on the criterion of CRF $\geq$ 90% considering the contamination by low and mid-level NO_2 and comparisons with the results of Pickering et al. (2016) and Lapierre et al. (2019).

3.2 Comparison of LNO_x Production based on Different AMFs

Lapierre et al. (2019) derived LNO_2 production based on the BEHR NO_2 product. In order for our results to be comparable with those of Pickering et al. (2016) and Lapierre et al. (2019), we choose NO_2 instead of NO_x to derive production per flash (production efficiency, PE). In Fig. 3, time series of NO_2Vis, LNO_2Vis, LNO_2 and LNO_2Clean production per day over CONUS are plotted for MJJA 2014 with the criterion of CRF $\geq$ 90% and a flash threshold of 2400 flashes per 2.4 h. LNO_2 production values are mostly in the range from 20 to 80 mol/flash. LNO_2Vis productions are smaller than LNO_2 productions which contain LNO_2 below clouds. The simulation of GMI in Pickering et al. (2016) indicated that 25% – 30% of the LNO_x column lies below the CP, while the ratio in our WRF-Chem simulation is $56 \pm 20\%$. The effect of cloud properties on LNO_x production will be discussed in more detail in section 3.4. Generally, the order of estimated daily PEs is LNO_2Clean > LNO_2 > NO_2Vis > LNO_2Vis. The percent difference in the estimated PE (ΔPE) between NO_2Vis and LNO_2Vis indicates a certain amount of background NO_2 exists above clouds. Overall, the tendency of that ΔPE is consistent with another ΔPE between NO_2Vis and LNO_2Clean. When the region is highly polluted (ΔPE between NO_2Vis and LNO_2 is larger than 200%), PEs based on NO_2Vis and LNO_2Clean are significantly overestimated. In other words, NO_2Vis and LNO_2Clean are more sensitive to background NO_2. The extent of the overestimation of NO_2Vis is larger than that of LNO_2Clean in highly polluted regions, while it is usually opposite in most regions.

Figure 4 shows the linear regression for ENTLN data versus NO_2Vis, LNO_2Vis, LNO_2 and LNO_2Clean with the same criteria as shown in Fig. 3. LNO_2Clean production (the largest slope) is 25.2 ± 22.3 mol NO_2/flash with a correlation of 0.25 and 2.3 ± 2.1 mol NO_2/stroke with a correlation of 0.22. As shown in Fig. 3, the number of positive percent differences between NO_2Vis and LNO_2Clean production is much fewer than that of negative differences. As a result, NO_2Vis production (17.1 ± 17.2 mol NO_2/flash and 0.4 ± 1.0 mol NO_2/stroke) is smaller than LNO_2Clean production using the linear regression method.

If the CP $\leq$ 650 hPa, TL $\geq$ 1000 and ratio $\geq$ 50% are removed from criteria, our result based on daily summed NO_2Vis values (3.8 ± 0.5 mol/stroke) is still larger than the value of 1.6 ± 0.1 mol/stroke mentioned in Lapierre et al. (2019). This may be caused by the different version of BEHR algorithm, as Lapierre et al. (2019) used BEHR V3.0A and our algorithm is based on BEHR V3.0B (Laughner et al., 2019). The input of S_{NO_2} in both versions is from the NASA standard product V3 and the major improvements of BEHR V3.0B are listed below:

1. The profile (V3.0B) closest to the OMI overpass time was selected instead of the last profile (V3.0A) before the OMI overpass.

2. The AMF uses a variable tropopause height as opposed to the fixed 200 hPa tropopause.

3. The surface pressure is now calculated according to Zhou et al. (2009).

The detailed log of changes is available at https://github.com/CohenBerkeleyLab/BEHR-core (last access: February 7, 2020). Note that Lapierre et al. (2019) used the monthly NO_2 profile, while the daily profile is used in our study and the interval of our

outputs from WRF-Chem is 30 min which is more frequent than 1 h in the BEHR daily product, the AMF could be affected by different NO_2 profiles. In view of these factors, we compare different methods based on our data to minimize these effects.

Meanwhile, LNO_2 production (18.7 $\pm$ 18.1 mol/flash and 2.1 $\pm$ 1.8 mol/stroke) is between LNO_2Clean production and NO_2Vis production, which coincides with the daily results in Fig. 3. Furthermore, the calculated LNO_x production based on daily summed values (not shown) is 114.8 $\pm$ 18.2 mol/flash (or 17.8 $\pm$ 2.9 mol/stroke) which is larger than 91 mol/flash from the linear regression result of Pickering et al. (2016), possibly due to the differences in geographic location, lightning data and chemistry model considered by Pickering et al. (2016) and this study.

The mean and standard deviation of LNO_2 production under CRF $\geq$ 90% using the summation method is 46.2 $\pm$ 35.1 mol/flash and 9.9 $\pm$ 8.1 mol/stroke, while LNO_x production is 125.6 $\pm$ 95.9 mol/flash and 26.7 $\pm$ 21.6 mol/stroke (Fig. 5). The LNO_2 and LNO_x production are both higher in the Southeast U.S. (denoted by the red box in Fig. 5 panels, 75°W – 95°W, 25°N – 37°N), consistent with Lapierre et al. (2019) and Bucsela et al. (2019). Compared with Fig. 3, Figure 6a and b present some large differences between NO_2Vis production and LNO_2Vis production, which are consistent with what we expect for polluted regions. Meanwhile, the differences between LNO_2 production and NO_2Vis production depend on background NO_2, the strength of updraft and the profile. The negative differences are caused by background NO_2 carried by the updraft while parts of the below-cloud LNO_2 results in more LNO_2 production estimates than NO_2Vis production estimates (Fig. 6c). Figure 6d shows that the ratio of LNO_2Vis to LNO_2 ranges from 10% – 80%. This may be caused by the height of the clouds and the profile of LNO_2. If the CP is near 300 hPa, the ratio should be smaller because of the coverage of clouds. The ratio would also be smaller while peaks of the LNO_2 profile are below the CP. Therefore, a better understanding of LNO_2 profile and LNO_x below clouds is required.

3.3 Effects of Tropospheric Background on LNO_x Production

The patterns in Fig. 6 indicate the improvement of our approach is different in polluted and clean regions. To simplify the quantification, we select six grids with similar NO_2 profile ($\sim$ 100 pptv) above the cloud with CRF = 100%. These grid boxes contain the cities denoted by stars and triangles in Fig. 6a. Then, the differences between AMFs are dependent on fewer parameters:

$$AMF_{\text{LNO}_2} = \frac{\int_{p_{cloud}}^{p_{tp}} w_{cloudy}(p) NO_2(p)\, dp}{\int_{p_{surf}}^{p_{tp}} LNO_2(p)\, dp} \tag{7}$$

$$AMF_{\text{NO}_2\text{Vis}} = \frac{\int_{p_{cloud}}^{p_{tp}} w_{cloudy}(p) NO_2(p)\, dp}{\int_{p_{cld}}^{p_{tp}} NO_2(p)\, dp} \tag{8}$$

$$AMF_{\text{LNO}_2\text{Clean}} = \frac{\int_{p_{cloud}}^{p_{tp}} w_{cloudy}(p) LNO_2(p)\, dp}{\int_{p_{surf}}^{p_{tp}} LNO_2(p)\, dp} \tag{9}$$

Figure 7 compares the mean profiles of NO_2, background NO_2 and background NO_2 ratio in polluted and clean grids. Generally, the profiles of background NO_2 ratio are C-shape because LNO_2 concentrations are higher than background NO_2 in the UT. However, the ratio profile in Fig. 7e has one peak between the cloud pressure and tropopause as background NO_2 increases and LNO_2 decreases. Besides, the percentage of UT background NO_2 in polluted regions is steady and higher than that in clean regions.

Table 4 presents the relative changes among three methods in six cities. The difference between AMF_{LNO_2} (Eq. 7) and AMF_{LNO_2Clean} (Eq. 9) is the numerator: $\int_{p_{cloud}}^{p_{tp}} w_{cloudy}(p)NO_2(p)\,dp$ and $\int_{p_{cloud}}^{p_{tp}} w_{cloudy}(p)LNO_2(p)\,dp$. When the ratio of LNO_2 is higher or the region is cleaner, the relative difference is smaller (e.g. 5.0% – 12.0%, Fig. 7d – f). The largest relative difference (46.3%) occurs when the ratio of background NO_2 is continuously high in the UT (Fig. 7c). As a result, our approach is less sensitive to background NO_2 and more suitable for convections over polluted locations. In contrast, production estimated by our method is larger than that based on NO_2 Vis due to the LNO_2 below the cloud. When the cloud is higher, especially the peak of LNO profile is lower than the cloud (Fig. 7b), the relative difference is larger (121.2%) because more LNO_2 can not be included into the NO_2 Vis, which has been discussed in Sect. 3.2. The relative change between AMF_{LNO_2Clean} (Eq. 9) and AMF_{NO_2Vis} (Eq. 8) depends on $\int_{p_{cloud}}^{p_{tp}} w_{cloudy}(p)LNO_2(p)\,dp / \int_{p_{surf}}^{p_{tp}} w_{cloudy}(p)LNO_2(p)\,dp$, which is also affected by cloud not the background NO_2. The largest relative change is 153.8% among the six grids where the highest clouds occur.

3.4 Effects of Cloud and LNO_x Parameterization on LNO_x Production

Figure 8a presents the daily distribution of CP and the ratio of LNO_2 Vis to LNO_2 during MJJA 2014 with the criteria defined in section 3.1 under CRF $\geq$ 90%. Since the ratio of LNO_2 Vis to LNO_2 decreases from 0.8 to 0.2 as the cloud pressure decreases from 600 to 300 hPa, NO_2 Vis production is smaller than LNO_2 in relatively clean areas as shown in Fig. 4. Apart from LNO_2 Vis, the LNO_2 production is also affected by CP. For LNO_2 production larger than 30 mol/stroke, the CPs are all smaller than 550 hPa (Fig. 8b). However, smaller LNO_2 production (< 30 mol/stroke) occurs on all levels between 650 hPa and 200 hPa. Because of the limited amount of large LNO_2 production and lightning data, we cannot derive the relationship between LNO_2 production and cloud pressure or different lightning properties at this stage. Because CP only represents the development of clouds, the vertical structure of flashes can not be derived from the CP values only. As discussed in several previous studies, flash channel length varies and depends on the environmental conditions (Carey et al., 2016; Mecikalski and Carey, 2017; Fuchs and Rutledge, 2018). Davis et al. (2019) compared two kinds of flashes: normal flashes and anomalous flashes. Because updrafts are stronger and flash rates are higher in anomalous storms, UT LNO_x concentrations is larger in anomalous than normal polarity storms. In general, normal flashes are coupled with an upper-level positive charge region and a mid-level negative charge region, while anomalous flashes are opposite (Williams, 1989). It is not straightforward to estimate the error resulting from the vertical distribution of LNO_x. There are mainly two methods of distributing LNO_x in models: LNO_x profiles (postconvection) in which LNO_x has already been redistributed by convective transport, while the other one (preconvection) uses LNO_x production profiles made before the redistribution of convective transport (Allen et al., 2012; Luo et al., 2017). However, given the similarity of results compared to other LNO_x studies, we believe that our $1° \times 1°$ results based on postconvective LNO_x profile are sufficient for estimating average LNO_x production.

The LNO production settings in WRF-Chem varied in different studies. Zhao et al. (2009) set a NO_x production rate of 250 mol NO per flash in a regional-scale model, while Bela et al. (2016) chose the same value (330 mol NO per flash) that was used by Barth et al. (2012). Wang et al. (2015) assumed approximately 500 mol NO per flash which was derived by a cloud-scale chemical transport model and in-cloud aircraft observations (Ott et al., 2010). To illustrate the impact of LNO_x parameterization on LNO_x estimation, we apply another WRF-Chem NO_2 profile setting ($2\times$base flashrate, 500 mol NO flash^{-1}; hereinafter referred to as "2×500 mol NO flash^{-1}") to a priori profiles and evaluate the changes in AMF_{LNO_2}, AMF_{LNO_x}, LNO_2 and LNO_x productions. For the linear regression method (Fig. 9), LNO_2 production is 29.8 ± 20.5 mol/flash which is 59.4% larger than the basic one (18.7 ± 18.1 mol/flash). Meanwhile, LNO_x production (increasing from 54.5 ± 48.1 mol/flash to 88.5 ± 61.1 mol/flash) also depends on the configuration of LNO production in WRF-Chem. It remains unclear as to whether the NO-NO_2-O_3 cycle or other LNO_x reservoirs accounts for the increment of LNO_x production. This would need detailed source analysis in WRF-Chem and is beyond the scope of this study.

Figure 10 shows the average percentage changes in AMF_{LNO_2}, AMF_{LNO_x}, LNO_2 and LNO_x between retrievals using profiles based on 1×200 mol NO flash^{-1} and 2×500 mol NO flash^{-1}. These results were obtained by averaging data over MJJA 2014 based on the method described in Sect. 2.5 with the criterion of CRF $\geq$ 90%. The effects on LNO_2 and LNO_x retrieval from increasing LNO profile values show mostly the same tendency: smaller AMF_{LNO_2} and AMF_{LNO_x} leads to larger LNO_2 and LNO_x, but the changes are regionally dependent. This is caused by the nonlinear calculation of AMF_{LNO_2} and AMF_{LNO_x}. As the contribution of LNO_2 increases, both the numerator and denominator of Eq. (2) increase. Note that the LNO_2 accounts for a fraction of NO_2 above the clouds, the magnitude of increasing denominator could be different than that of increasing numerator, resulting in a different effect on the AMF_{LNO_2} and AMF_{LNO_x}. As mentioned in Zhu et al. (2019), the lightning densities in the Southeast U.S. might be overestimated using the 2×500 mol NO flash^{-1} setting and the same lightning parameterization as ours. Fortunately, the AMFs and estimated LNO_2 change little in that region.

Figure 11 shows the comparison of the mean LNO and LNO_2 profiles in two specific regions where the 2×500 mol NO flash^{-1} setting leads to both lower and higher LNO_2 production. The first one (Fig. 11a) is the region ($36°N – 37°N$, $89°W – 90°W$) containing the minimal negative percent change in LNO_2 (Fig. 10c). The second one ($31°N – 32°N$, $97°W – 98°W$), Figure 11b, has the largest positive percent change in LNO_2 (Fig. 10c). Although the relative distributions of mean LNO and LNO_2 profiles are similar in both regions, the magnitude differs with a factor of 10. This phenomenon implies that the performance of lightning parameterization in WRF-Chem is region dependent and an unrealistic profile could appear in the UT. Although this sensitivity analysis is false in some regions, it allows the calculation of an upper limit on the NO_2 due to LNO and LNO_2 profiles. As discussed in Laughner and Cohen (2017), the scattering weights are uniform under cloudy conditions and the sensitivity of NO_2 is nearly constant with different pressure levels because of the high albedo. However, the relative distribution of LNO_2 within the UT should be taken carefully into consideration. If the LNO_2/NO_2 above the cloud is large enough (Fig. 11a), the AMF_{LNO_2} is largely determined by the ratio of LNO_2 Vis to LNO_2 which is related to the relative distribution. When the condition of high LNO_2/NO_2 is not met, both relative distribution and ratio are important (Fig. 11b).

To clarify this, we applied the same sensitivity test of different simulating LNO amounts for all four methods mentioned in Sect. 2.4: LNO_2, LNO_2 Vis, LNO_2 Clean and NO_2 Vis (Fig. 12). Note that the threshold for CRF is set to 100% to simplify Eq.

(2) to Eq. (7). The overall differences of LNO$_2$Clean and NO$_2$Vis are smaller than those of LNO$_2$ and LNO$_2$Vis. Comparing the composition of numerator and denominator in the equations, it is clear why the impact of different simulating LNO amounts is smaller in Fig. 12c and d. For LNO$_2$Clean and NO$_2$Vis, both the SCD and VCD will increase (decrease) when more (less) LNO$_2$ or NO$_2$ presents. The difference between Fig. 12a and Fig. 12b is the denominator: the total tropospheric LNO$_2$ vertical column and visible LNO$_2$ vertical column respectively. As a result, the negative values in Fig. 12a is caused by the part of LNO$_2$ below the cloud. The comparison between Fig. 4 and Fig. 9 shows that LNO$_2$Clean and LNO$_2$ values are more similar while LNO$_2$ and NO$_2$Vis values are same. The uncertainty of retrieved LNO$_2$ and LNO$_x$ productions is driven by this error, and we conservatively estimate this to be $\pm$ 15% and $\pm$ 29% respectively.

4 Uncertainties Analysis

The uncertainties of the LNO$_2$ and LNO$_x$ production are estimated following Pickering et al. (2016), Allen et al. (2019), Bucsela et al. (2019), Lapierre et al. (2019) and Laughner et al. (2019). We determine the uncertainty due to BEHR tropopause pressure, cloud radiance fraction, cloud pressure, surface pressure, surface reflectivity, profile shape, profile location, V$_{strat}$, the detection efficiency of lightning, t$_{window}$ and LNO$_2$ lifetime numerically by perturbing each parameter in turn and re-retrieval of the LNO$_2$ and LNO$_x$ with the perturbed values (Table 5).

The GEOS-5 monthly tropopause pressure, which is consistent with the NASA Standard Product, is applied instead of the variable WRF tropopause height to evaluate the uncertainty (6% for LNO$_2$ and 4% for LNO$_x$) caused by the BEHR tropopause pressure. Beirle et al. (2009) obtained a mean total sensitivity of 0.46 (σ = 0.09) for LNO$_x$ in the sensitivity study, implying an uncertainty of 23% due to cloud pressure in our study. The resolution of GLOBE terrain height data is much higher than the OMI pixel and a fixed scale height is assumed in the BEHR algorithm. As a result, Laughner et al. (2019) compared the average WRF surface pressures to the GLOBE surface pressures and arrived at the largest bias of 1.5%. Based on the largest bias, we vary the surface pressure (limited to less than 1020 hPa) and the uncertainty can be neglected.

The error in cloud radiance fraction is transformed from cloud fraction using:

$$\sigma = 0.05 \cdot \left. \frac{\partial f_r}{\partial f_g} \right|_{f_{g,pix}} \tag{10}$$

where f_r is the cloud radiance fraction, f_g is the cloud fraction and $f_{g,pix}$ is the cloud fraction of a specific pixel. We calculate $\partial f_r / \partial f_g$ under $f_{g,pix}$ by the relationship between all binned f_r and f_g with the increment of 0.05 for the each specific OMI orbit. Considering the relationship, the error in cloud fraction is converted to an error in cloud radiance fraction of 2% for both LNO$_2$ and LNO$_x$.

The accuracy of the 500 m MODIS albedo product is usually within 5% of albedo observations at the validation sites and those exceptions with low quality flags have been found to be primarily within 10% of the field data (Schaaf et al., 2011). Since we use the bidirectional reflectance distribution function (BRDF) data directly, rather than including a radiative transfer model, 14% Lambertian equivalent reflectivity (LER) error and 10% uncertainty are combined to get a perturbation of 17% (Laughner et al., 2019). The uncertainty due to surface reflectivity can be neglected with the 17% perturbation.

As discussed at the end of Sect. 3.4, another setting of LNO_2 (2×500 mol NO flash^{-1}) is applied to determine the uncertainty of the lightning parameterization and the vertical distribution of LNO in WRF-Chem. Differences between the two profiles lead to an uncertainty of 15% and 29%in the resulting LNO_2 and LNO_x production. Another sensitivity test allows each pixel to shift by - 0.2, 0, or + 0.2 degrees in the directions of longitude and latitude, taking advantage of the high-resolution profile location in WRF-Chem. The resulting uncertainty of LNO_x production is 1% including the error of transport and chemistry by shifting pixels.

Compared to the NASA standard product v2, Krotkov et al. (2017) demonstrated that the noise in V_{strat} is 1×10^{14} cm^{-2}. Errors in polluted regions can be slightly larger than this value, while errors in the cleanest areas are typically significantly smaller (Bucsela et al., 2013). We estimated the uncertainty of V_{strat} component and the slant column errors to be 10% and 5%, respectively, following Allen et al. (2019).

Based on the standard deviation of the detection efficiency estimation over the CONUS relative to LIS, ENTLN detection efficiency uncertainties are $\pm$ 16% for total and IC flashes/strokes. Due to the high detection efficiency of CG over the CONUS, the uncertainty is estimated to be $\pm$ 5% (Lapierre et al., 2019). It is found that the resulting uncertainty of detection efficiency is 15% in the production analysis. We have used the t_{window} of 2.4 h for counting ENTLN flashes and strokes to analyze LNO_2 and LNO_x production. Because t_{window} derived from the ERA5 reanalysis can not represent the variable wind speeds, a sensitivity test is performed which yields an uncertainty of 10% for production per flash and 8% for production per stroke using t_{window} of 2 h and 4 h. Meanwhile, the lifetime of UT NO_x ranges from 2 hours to 12 hours depending on the convective location, the methyl peroxy nitrate and alkyl and multifunctional nitrates (Nault et al., 2017). The lifetime (τ) of NO_2 in Eq. (6) is replaced by 2 and 12 hours to determine the uncertainty as 24% due to lifetime. The lifetime is the most likely uncertainty in the production analysis of LNO_2 while the uncertainty caused by lightning parameterization is comparable with that for the LNO_x type.

Recent works revealed that the modeled NO/NO_2 ratio departs from the data in the SEAC^{4}RS aircraft campaign (Travis et al., 2016; Silvern et al., 2018). Silvern et al. (2018) attributed this to the positive interference on the NO_2 measurements or errors in the cold-temperature $NO-NO_2-O_3$ photochemical reaction rate. We assign an uncertainty of 20% to this error considering the possible positive NO_2 measurements interferences (Allen et al., 2019; Bucsela et al., 2019).

In addition, the estimation of LNO_x PE is also dependent on the tropospheric background NO_2. In our method, main factors affecting this factor are the emissions inventory and the amount of transported NO_2. For the emissions inventory, the sources of uncertainty are assumptions, methods, input data and calculation errors. As a result, the uncertainties for different species or pollutants related to NO_2 are different and EPA also doesn't publish the quantified uncertainty measures because the parties that submit emissions estimates to EPA are not asked to include quantitative uncertainty measurements or estimates (EPA, 2015). For the simulated convective transport, Li et al. (2018) compared the cloud-resolving simulations with these based on convective parameterization and pointed out that the convective transport was weaker in the parameterization. But, we believe that the ratio condition ($LNO_2 Vis/NO_2 Vis \geq 50\%$) should reduce these two kinds of uncertainty and assume an uncertainty of 10%, which is less than 20% assigned in Allen et al. (2019) and Bucsela et al. (2019).

The overall uncertainty is estimated as the square root of the sum of the squares of all individual uncertainties in Table 5. The net uncertainty is 48% and 54% for LNO_2 type and LNO_x type respectively. The mean LNO_2/flash, LNO_x/flash, LNO_2/stroke, LNO_x/stroke based on the linear regression and summation method are 32 mol/flash, 90 mol/flash, 6 mol/stroke and 17 mol/stroke. Applying the corresponding uncertainty to these mean values, we arrive at 32 ± 15 mol LNO_2/flash, 90 ± 49 mol LNO_x/flash, 6 ± 3 mol LNO_2/stroke and 17 ± 9 mol LNO_x/stroke. This is in the range of current literature estimate ranging from 33 to 500 mol LNO_x/flash (Schumann and Huntrieser, 2007; Beirle et al., 2010; Bucsela et al., 2010). Bucsela et al. (2010) estimated LNO_x production of $100 - 250$ mol/flash which is similar to our flash-based results. Pickering et al. (2016) estimated LNO_x production to be 80 ± 45 mol per flash for the Gulf of Mexico, which is 50% smaller than our flash-based results over the CONUS. Note that the criteria defined in Sect. 3.1 lead to many missing data over the Gulf of Mexico, thus it is actually a comparison between different regions. For the stroke-based results, Lapierre et al. (2019) yields lower LNO_2 production of 1.6 ± 0.1 mol per stroke, the difference is caused by the different version of BEHR algorithm and several settings as mentioned in Sect. 3.2. Bucsela et al. (2019) inferred an average value of 200 ± 110 moles (67% larger than our results) LNO_x produced per flash over the North America, this is related to the different algorithm and lightning data.

5   Conclusions

In this study, a new algorithm for retrieving LNO_2 (LNO_x) from OMI, including LNO_2 (LNO_x) below cloud, has been developed for application over active convection. It works in both clean and polluted regions because of the consideration of tropospheric background pollution in the definition of AMFs. It uses specific criteria combining with several other conditions (sufficient CRF, coincident ENTLN data, TL $\geq$ 1000 and ratio $\geq$ 50%) to ensure that the electrically active regions are detected by OMI and simulated by WRF-Chem successfully. We conducted an analysis on $1° \times 1°$ daily boxes in MJJA 2014 and obtained the seasonal mean LNO_2 and LNO_x production efficiencies over the CONUS. Considering all the uncertainties (Table 5) and applying the summation and regression method, the final mean production efficiencies are estimated to be 32 ± 15 mol LNO_2/flash, 90 ± 49 mol LNO_x/flash, 6 ± 3 mol LNO_2/stroke and 17 ± 9 mol LNO_x/stroke.

Compared with former methods, our method has reduced the sensitive to background NO_2, while the method in Lapierre et al. (2019) underestimates LNO_x production efficiency because of the neglected below-cloud LNO_2 and LNO_2 production is overestimated using the method in Pickering et al. (2016) due to the over-cloud background NO_2 in polluted regions. Finally, implementing profiles generated with different model settings of lightning (1×200 mol NO flash^{-1} and 2×500 mol NO flash^{-1}), we find that the larger LNO production model setting leads to larger retrieval of LNO_x despite some regionally dependent effects caused by nonlinear calculation of AMF. Both the ratio of the tropospheric LNO_2 above the cloud to the total tropospheric LNO_2 and the ratio of LNO_2 to NO_2 cause different comprehensive effects due to the nonlinear calculation of AMF_{LNO_2} and AMF_{LNO_x}.

Since other regions, like China and India, have much more NO_2 pollution than the CONUS, it is necessary to consider the background NO_2 in detail. These analyses will be complemented by the recently launched satellite instrument (TROPOspheric Monitoring Instrument [TROPOMI]) (Veefkind et al., 2012; Boersma et al., 2018; Griffin et al., 2019) and Lightning Mapping

Imager (LMI) on the new generation Chinese geostationary meteorological satellites Fengyun-4 (Min et al., 2017; Yang et al., 2017; Zhang et al., 2019). Future work investigating the flash channel length and more detailed lightning parameterization in WRF-Chem would greatly benefit LNO_x estimation. Applying current method in future studies may enhance the accuracy of LNO_x production at both local and global scales.

Code and data availability. The retrieval algorithm used in Sect. 2.4 is available at https://github.com/zxdawn/BEHR-LNOx (last access:
480 February 7, 2020; Zhang and Laughner, 2019). The WRF-Chem model output and LNO_x product are available upon request to Xin Zhang (xinzhang1215@gmail.com).

Appendix A: AMF Definitions used in this Study

$$AMF_{\mathrm{LNO_2}} = \frac{(1-f_r)\int_{p_{surf}}^{p_{tp}} w_{clear}(p)NO_2(p)\,dp + f_r \int_{p_{cloud}}^{p_{tp}} w_{cloudy}(p)NO_2(p)\,dp}{\int_{p_{surf}}^{p_{tp}} LNO_2(p)\,dp} \tag{A1}$$

$$AMF_{\mathrm{LNO}_x} = \frac{(1-f_r)\int_{p_{surf}}^{p_{tp}} w_{clear}(p)NO_2(p)\,dp + f_r \int_{p_{cloud}}^{p_{tp}} w_{cloudy}(p)NO_2(p)\,dp}{\int_{p_{surf}}^{p_{tp}} LNO_x(p)\,dp} \tag{A2}$$

485 where f_r is the radiance cloud fraction, p_{surf} is the surface pressure, p_{tp} is the tropopause pressure, p_{cloud} is the cloud optical pressure (CP), w_{clear} and w_{cloudy} are respectively the pressure dependent scattering weights from the TOMRAD lookup table (Bucsela et al., 2013) for clear and cloudy parts, and $NO_2(p)$ is the modeled NO_2 vertical profile. $LNO_2(p)$ and $LNO_x(p)$ are respectively the LNO_2 and LNO_x vertical profile calculated by the difference of vertical profiles between WRF-Chem simulations with and without lightning.

$$AMF_{\mathrm{LNO_2\,Clean}} = \frac{(1-f_r)\int_{p_{surf}}^{p_{tp}} w_{clear}(p)LNO_2(p)\,dp + f_r \int_{p_{cloud}}^{p_{tp}} w_{cloudy}(p)LNO_2(p)\,dp}{\int_{p_{surf}}^{p_{tp}} LNO_2(p)\,dp} \tag{A3}$$

$$AMF_{\mathrm{NO_2\,Vis}} = \frac{(1-f_r)\int_{p_{surf}}^{p_{tp}} w_{clear}(p)NO_2(p)\,dp + f_r \int_{p_{cloud}}^{p_{tp}} w_{cloudy}(p)NO_2(p)\,dp}{(1-f_g)\int_{p_{surf}}^{p_{tp}} NO_2(p)\,dp + f_g \int_{p_{cloud}}^{p_{tp}} NO_2(p)\,dp} \tag{A4}$$

$$AMF_{\mathrm{NO}_x\,\mathrm{Vis}} = \frac{(1-f_r)\int_{p_{surf}}^{p_{tp}} w_{clear}(p)NO_2(p)\,dp + f_r \int_{p_{cloud}}^{p_{tp}} w_{cloudy}(p)NO_2(p)\,dp}{(1-f_g)\int_{p_{surf}}^{p_{tp}} NO_x(p)\,dp + f_g \int_{p_{cloud}}^{p_{tp}} NO_x(p)\,dp} \tag{A5}$$

$$AMF_{\mathrm{LNO_2\,Vis}} = \frac{(1-f_r)\int_{p_{surf}}^{p_{tp}} w_{clear}(p)NO_2(p)\,dp + f_r \int_{p_{cloud}}^{p_{tp}} w_{cloudy}(p)NO_2(p)\,dp}{(1-f_g)\int_{p_{surf}}^{p_{tp}} LNO_2(p)\,dp + f_g \int_{p_{cloud}}^{p_{tp}} LNO_2(p)\,dp} \tag{A6}$$

where f_g is the geometric cloud fraction and $NO_x(p)$ is the modeled NO_x vertical profile.

References

Acarreta, J. R., de Haan, J. F., and Stammes, P.: Cloud pressure retrieval using the O_2 -O_2 absorption band at 477 nm, Journal of Geophysical Research, 109, 2165, https://doi.org/10.1029/2003JD003915, 2004.

Allen, D. J., Pickering, K. E., Duncan, B. N., and Damon, M.: Impact of lightning NO emissions on North American photochemistry as determined using the Global Modeling Initiative (GMI) model, Journal of Geophysical Research, 115, 4711, https://doi.org/10.1029/2010JD014062, 2010.

Allen, D. J., Pickering, K. E., Pinder, R. W., Henderson, B. H., Appel, K. W., and Prados, A.: Impact of lightning-NO on eastern United States photochemistry during the summer of 2006 as determined using the CMAQ model, Atmospheric Chemistry and Physics, 12, 1737–1758, https://doi.org/10.5194/acp-12-1737-2012, 2012.

Allen, D. J., Pickering, K. E., Bucsela, E. J., Krotkov, N., and Holzworth, R.: Lightning NO_x Production in the Tropics as Determined Using OMI NO_2 Retrievals and WWLLN Stroke Data, Journal of Geophysical Research: Atmospheres, https://doi.org/10.1029/2018JD029824, 2019.

Banerjee, A., Archibald, A. T., Maycock, A. C., Telford, P., Abraham, N. L., Yang, X., Braesicke, P., and Pyle, J. A.: Lightning NO_x, a key chemistry–climate interaction: impacts of future climate change and consequences for tropospheric oxidising capacity, Atmospheric Chemistry and Physics, 14, 9871–9881, https://doi.org/10.5194/acp-14-9871-2014, 2014.

Barth, M. C., Lee, J., Hodzic, A., Pfister, G., Skamarock, W. C., Worden, J., Wong, J., and Noone, D.: Thunderstorms and upper troposphere chemistry during the early stages of the 2006 North American Monsoon, Atmospheric Chemistry and Physics, 12, 11 003–11 026, https://doi.org/10.5194/acp-12-11003-2012, 2012.

Beirle, S., Platt, U., Wenig, M., and Wagner, T.: NO_x production by lightning estimated with GOME, Advances in Space Research, 34, 793–797, https://doi.org/10.1016/j.asr.2003.07.069, 2004.

Beirle, S., Spichtinger, N., Stohl, A., Cummins, K. L., Turner, T., Boccippio, D., Cooper, O. R., Wenig, M., Grzegorski, M., Platt, U., and Wagner, T.: Estimating the NO_x produced by lightning from GOME and NLDN data: A case study in the Gulf of Mexico, Atmospheric Chemistry and Physics, 6, 1075–1089, https://doi.org/10.5194/acp-6-1075-2006, 2006.

Beirle, S., Salzmann, M., Lawrence, M. G., and Wagner, T.: Sensitivity of satellite observations for freshly produced lightning NO x, Atmospheric Chemistry and Physics, 9, 1077–1094, https://doi.org/10.5194/acp-9-1077-2009, 2009.

Beirle, S., Huntrieser, H., and Wagner, T.: Direct satellite observation of lightning-produced NO_x, Atmospheric Chemistry and Physics, 10, 10 965–10 986, https://doi.org/10.5194/acp-10-10965-2010, 2010.

Bela, M. M., Barth, M. C., Toon, O. B., Fried, A., Homeyer, C. R., Morrison, H., Cummings, K. A., Li, Y., Pickering, K. E., Allen, D. J., Yang, Q., Wennberg, P. O., Crounse, J. D., St. Clair, J. M., Teng, A. P., O'Sullivan, D., Huey, L. G., Chen, D., Liu, X., Blake, D. R., Blake, N. J., Apel, E. C., Hornbrook, R. S., Flocke, F., Campos, T., and Diskin, G.: Wet scavenging of soluble gases in DC3 deep convective storms using WRF-Chem simulations and aircraft observations, Journal of Geophysical Research: Atmospheres, 121, 4233–4257, https://doi.org/10.1002/2015JD024623, 2016.

Boersma, K. F., Eskes, H. J., Meijer, E. W., and Kelder, H. M.: Estimates of lightning NO_x production from GOME satellite observations, Atmospheric Chemistry and Physics, 5, 2311–2331, https://doi.org/10.5194/acp-5-2311-2005, 2005.

Boersma, K. F., Eskes, H. J., Richter, A., de Smedt, I., Lorente, A., Beirle, S., van Geffen, J. H. G. M., Zara, M., Peters, E., van Roozendael, M., Wagner, T., d. Maasakkers, J., van der A, R. J., Nightingale, J., de Rudder, A., Irie, H., Pinardi, G., Lambert, J.-C., and Compernolle, S. C.: Improving algorithms and uncertainty estimates for satellite NO_2 retrievals: results from the quality assurance for the essential

climate variables (QA4ECV) project, Atmospheric Measurement Techniques, 11, 6651–6678, https://doi.org/10.5194/amt-11-6651-2018, 2018.

Bovensmann, H., Burrows, J. P., Buchwitz, M., Frerick, J., Noël, S., Rozanov, V. V., Chance, K. V., and Goede, A. P. H.: SCIA-MACHY: Mission Objectives and Measurement Modes, Journal of the Atmospheric Sciences, 56, 127–150, https://doi.org/10.1175/1520-0469(1999)056<0127:SMOAMM>2.0.CO;2, 1999.

Browne, E. C., Wooldridge, P. J., Min, K.-E., and Cohen, R. C.: On the role of monoterpene chemistry in the remote continental boundary layer, Atmospheric Chemistry and Physics, 14, 1225–1238, https://doi.org/10.5194/acp-14-1225-2014, 2014.

Bucsela, E. J., Pickering, K. E., Huntemann, T. L., Cohen, R. C., Perring, A., Gleason, J. F., Blakeslee, R. J., Albrecht, R. I., Holzworth, R., Cipriani, J. P., Vargas-Navarro, D., Mora-Segura, I., Pacheco-Hernández, A., and Laporte-Molina, S.: Lightning-generated NO_x seen by the Ozone Monitoring Instrument during NASA's Tropical Composition, Cloud and Climate Coupling Experiment (TC[4]), Journal of Geophysical Research, 115, 793, https://doi.org/10.1029/2009JD013118, 2010.

Bucsela, E. J., Krotkov, N. A., Celarier, E. A., Lamsal, L. N., Swartz, W. H., Bhartia, P. K., Boersma, K. F., Veefkind, J. P., Gleason, J. F., and Pickering, K. E.: A new stratospheric and tropospheric NO_2 retrieval algorithm for nadir-viewing satellite instruments: Applications to OMI, Atmospheric Measurement Techniques, 6, 2607–2626, https://doi.org/10.5194/amt-6-2607-2013, 2013.

Bucsela, E. J., Pickering, K. E., Allen, D. J., Holzworth, R., and Krotkov, N. A.: Midlatitude lightning NO_x production efficiency inferred from OMI and WWLLN data, Journal of Geophysical Research: Atmospheres, https://doi.org/10.1029/2019JD030561, 2019.

Burrows, J. P., Weber, M., Buchwitz, M., Rozanov, V., Ladstätter-Weißenmayer, A., Richter, A., DeBeek, R., Hoogen, R., Bramstedt, K., Eichmann, K.-U., Eisinger, M., and Perner, D.: The Global Ozone Monitoring Experiment (GOME): Mission Concept and First Scientific Results, Journal of the Atmospheric Sciences, 56, 151–175, https://doi.org/10.1175/1520-0469(1999)056<0151:TGOMEG>2.0.CO;2, 1999.

Callies, J., Corpaccioli, E., Eisinger, M., Hahne, A., and Lefebvre, A.: GOME-2-Metop's second-generation sensor for operational ozone monitoring, ESA bulletin, 102, 28–36, 2000.

Carey, L. D., Koshak, W., Peterson, H., and Mecikalski, R. M.: The kinematic and microphysical control of lightning rate, extent, and NO X production, Journal of Geophysical Research: Atmospheres, 121, 7975–7989, https://doi.org/10.1002/2015JD024703, 2016.

Choi, S., Joiner, J., Choi, Y., Duncan, B. N., Vasilkov, A., Krotkov, N., and Bucsela, E.: First estimates of global free-tropospheric NO_2 abundances derived using a cloud-slicing technique applied to satellite observations from the Aura Ozone Monitoring Instrument (OMI), Atmospheric Chemistry and Physics, 14, 10 565–10 588, https://doi.org/10.5194/acp-14-10565-2014, 2014.

Clark, S. K., Ward, D. S., and Mahowald, N. M.: Parameterization-based uncertainty in future lightning flash density, Geophysical Research Letters, 44, 2893–2901, https://doi.org/10.1002/2017GL073017, 2017.

Davis, T. C., Rutledge, S. A., and Fuchs, B. R.: Lightning location, NOx production, and transport by anomalous and normal polarity thunderstorms, Journal of Geophysical Research: Atmospheres, https://doi.org/10.1029/2018JD029979, 2019.

DeCaria, A. J., Pickering, K. E., Stenchikov, G. L., Scala, J. R., Stith, J. L., Dye, J. E., Ridley, B. A., and Laroche, P.: A cloud-scale model study of lightning-generated NO_x in an individual thunderstorm during STERAO-A, Journal of Geophysical Research, 105, 11 601–11 616, https://doi.org/10.1029/2000JD900033, 2000.

DeCaria, A. J., Pickering, K. E., Stenchikov, G. L., and Ott, L. E.: Lightning-generated NO_x and its impact on tropospheric ozone production: A three-dimensional modeling study of a Stratosphere-Troposphere Experiment: Radiation, Aerosols and Ozone (STERAO-A) thunderstorm, Journal of Geophysical Research, 110, n/a–n/a, https://doi.org/10.1029/2004JD005556, 2005.

580   Dobber, M., Kleipool, Q., Dirksen, R., Levelt, P., Jaross, G., Taylor, S., Kelly, T., Flynn, L., Leppelmeier, G., and Rozemeijer, N.: Validation of Ozone Monitoring Instrument level 1b data products, Journal of Geophysical Research, 113, 5224, https://doi.org/10.1029/2007JD008665, 2008.

Emmons, L. K., Walters, S., Hess, P. G., Lamarque, J.-F., Pfister, G. G., Fillmore, D., Granier, C., Guenther, A., Kinnison, D., Laepple, T., Orlando, J., Tie, X., Tyndall, G., Wiedinmyer, C., Baughcum, S. L., and Kloster, S.: Description and evaluation of the Model for Ozone and
585   Related chemical Tracers, version 4 (MOZART-4), Geoscientific Model Development, 3, 43–67, https://doi.org/10.5194/gmd-3-43-2010, 2010.

EPA, U.: 2011 National Emissions Inventory, version 2—Technical support document, US Environmental Protection Agency, Office of Air Quality Planning and Standards. Accessed August 2017., 2015.

EPA, U. S. and OAR: Air Pollutant Emissions Trends Data | US EPA, https://www.epa.gov/air-emissions-inventories/
590   air-pollutant-emissions-trends-data, 2015.

Finney, D. L., Doherty, R. M., Wild, O., Young, P. J., and Butler, A.: Response of lightning NO x emissions and ozone production to climate change: Insights from the Atmospheric Chemistry and Climate Model Intercomparison Project, Geophysical Research Letters, 43, 5492–5500, https://doi.org/10.1002/2016GL068825, 2016.

Finney, D. L., Doherty, R. M., Wild, O., Stevenson, D. S., MacKenzie, I. A., and Blyth, A. M.: A projected decrease in lightning under
595   climate change, Nature Climate Change, 8, 210–213, https://doi.org/10.1038/s41558-018-0072-6, 2018.

Fried, A., Barth, M. C., Bela, M., Weibring, P., Richter, D., Walega, J., Li, Y., Pickering, K., Apel, E., Hornbrook, R., Hills, A., Riemer, D. D., Blake, N., Blake, D. R., Schroeder, J. R., Luo, Z. J., Crawford, J. H., Olson, J., Rutledge, S., Betten, D., Biggerstaff, M. I., Diskin, G. S., Sachse, G., Campos, T., Flocke, F., Weinheimer, A., Cantrell, C., Pollack, I., Peischl, J., Froyd, K., Wisthaler, A., Mikoviny, T., and Woods, S.: Convective transport of formaldehyde to the upper troposphere and lower stratosphere and associated scavenging in
600   thunderstorms over the central United States during the 2012 DC3 study, Journal of Geophysical Research: Atmospheres, 121, 7430–7460, https://doi.org/10.1002/2015JD024477, 2016.

Fuchs, B. R. and Rutledge, S. A.: Investigation of Lightning Flash Locations in Isolated Convection Using LMA Observations, Journal of Geophysical Research: Atmospheres, 123, 6158–6174, https://doi.org/10.1002/2017JD027569, 2018.

Goliff, W. S., Stockwell, W. R., and Lawson, C. V.: The regional atmospheric chemistry mechanism, version 2, Atmospheric Environment,
605   68, 174–185, https://doi.org/10.1016/j.atmosenv.2012.11.038, 2013.

Grell, G. A., Peckham, S. E., Schmitz, R., McKeen, S. A., Frost, G., Skamarock, W. C., and Eder, B.: Fully coupled "online" chemistry within the WRF model, Atmospheric Environment, 39, 6957–6975, https://doi.org/10.1016/j.atmosenv.2005.04.027, 2005.

Griffin, D., Zhao, X., McLinden, C. A., Boersma, F., Bourassa, A., Dammers, E., Degenstein, D., Eskes, H., Fehr, L., Fioletov, V., Hayden, K., Kharol, S. K., Li, S.-M., Makar, P., Martin, R. V., Mihele, C., Mittermeier, R. L., Krotkov, N., Sneep, M., Lamsal, L. N., Linden, M. t.,
610   van Geffen, J., Veefkind, P., and Wolde, M.: High-Resolution Mapping of Nitrogen Dioxide With TROPOMI: First Results and Validation Over the Canadian Oil Sands, Geophysical Research Letters, 46, 1049–1060, https://doi.org/10.1029/2018GL081095, 2019.

Guenther, A., Karl, T., Harley, P., Wiedinmyer, C., Palmer, P. I., and Geron, C.: Estimates of global terrestrial isoprene emissions using MEGAN (Model of Emissions of Gases and Aerosols from Nature), Atmospheric Chemistry and Physics, 6, 3181–3210, https://hal.archives-ouvertes.fr/hal-00295995, 2006.

615   Hauglustaine, D., Emmons, L., Newchurch, M., Brasseur, G., Takao, T., Matsubara, K., Johnson, J., Ridley, B., Stith, J., and Dye, J.: On the Role of Lightning NO_x in the Formation of Tropospheric Ozone Plumes: A Global Model Perspective, Journal of Atmospheric Chemistry, 38, 277–294, https://doi.org/10.1023/A:1006452309388, 2001.

Joiner, J., Vasilkov, A. P., Gupta, P., Bhartia, P. K., Veefkind, P., Sneep, M., de Haan, J., Polonsky, I., and Spurr, R.: Fast simulators for satellite cloud optical centroid pressure retrievals; evaluation of OMI cloud retrievals, Atmospheric Measurement Techniques, 5, 529–545, https://doi.org/10.5194/amt-5-529-2012, 2012.

KNMI: Background information about the Row Anomaly in OMI, http://projects.knmi.nl/omi/research/product/rowanomaly-background.php, last access: February 7, 2020, 2012.

Krause, A., Kloster, S., Wilkenskjeld, S., and Paeth, H.: The sensitivity of global wildfires to simulated past, present, and future lightning frequency, Journal of Geophysical Research: Biogeosciences, 119, 312–322, https://doi.org/10.1002/2013JG002502, 2014.

Krotkov, N. A., Lamsal, L. N., Celarier, E. A., Swartz, W. H., Marchenko, S. V., Bucsela, E. J., Chan, K. L., Wenig, M., and Zara, M.: The version 3 OMI NO_2 standard product, Atmospheric Measurement Techniques, 10, 3133–3149, https://doi.org/10.5194/amt-10-3133-2017, 2017.

Kuhlmann, G., Hartl, A., Cheung, H. M., Lam, Y. F., and Wenig, M. O.: A novel gridding algorithm to create regional trace gas maps from satellite observations, Atmospheric Measurement Techniques, 7, 451–467, https://doi.org/10.5194/amt-7-451-2014, 2014.

Lapierre, J. L., Laughner, J. L., Geddes, J. A., Koshack, W., Cohen, R. C., and Pusede, S. E.: Observing regional variability in lightning NO_x production rates, Journal of Geophysical Research, in review, 2019.

Laughner, J. L. and Cohen, R. C.: Quantification of the effect of modeled lightning NO_2 on UV–visible air mass factors, Atmospheric Measurement Techniques, 10, 4403–4419, https://doi.org/10.5194/amt-10-4403-2017, 2017.

Laughner, J. L., Zhu, Q., and Cohen, R. C.: The Berkeley High Resolution Tropospheric NO_2 Product, Earth System Science Data Discussions, pp. 1–33, https://doi.org/10.5194/essd-2018-66, 2018a.

Laughner, J. L., Zhu, Q., and Cohen, R. C.: Evaluation of version 3.0B of the BEHR OMI NO_2 product, Atmospheric Measurement Techniques Discussions, pp. 1–25, https://doi.org/10.5194/amt-2018-248, 2018b.

Laughner, J. L., Zhu, Q., and Cohen, R. C.: Evaluation of version 3.0B of the BEHR OMI NO_2 product, Atmospheric Measurement Techniques, 12, 129–146, https://doi.org/10.5194/amt-12-129-2019, 2019.

Levelt, P. F., van den Oord, G., Dobber, M. R., Malkki, A., Visser, H., Vries, J. d., Stammes, P., Lundell, J., and Saari, H.: The ozone monitoring instrument, IEEE Transactions on Geoscience and Remote Sensing, 44, 1093–1101, https://doi.org/10.1109/TGRS.2006.872333, 2006.

Levelt, P. F., Joiner, J., Tamminen, J., Veefkind, J. P., Bhartia, P. K., Stein Zweers, D. C., Duncan, B. N., Streets, D. G., Eskes, H., van der A, R., McLinden, C., Fioletov, V., Carn, S., de Laat, J., DeLand, M., Marchenko, S., McPeters, R., Ziemke, J., Fu, D., Liu, X., Pickering, K., Apituley, A., González Abad, G., Arola, A., Boersma, F., Chan Miller, C., Chance, K., de Graaf, M., Hakkarainen, J., Hassinen, S., Ialongo, I., Kleipool, Q., Krotkov, N., Li, C., Lamsal, L., Newman, P., Nowlan, C., Suleiman, R., Tilstra, L. G., Torres, O., Wang, H., and Wargan, K.: The Ozone Monitoring Instrument: overview of 14 years in space, Atmospheric Chemistry and Physics, 18, 5699–5745, https://doi.org/10.5194/acp-18-5699-2018, 2018.

Li, Y., Pickering, K. E., Allen, D. J., Barth, M. C., Bela, M. M., Cummings, K. A., Carey, L. D., Mecikalski, R. M., Fierro, A. O., Campos, T. L., Weinheimer, A. J., Diskin, G. S., and Biggerstaff, M. I.: Evaluation of deep convective transport in storms from different convective regimes during the DC3 field campaign using WRF-Chem with lightning data assimilation, Journal of Geophysical Research: Atmospheres, 122, 7140–7163, https://doi.org/10.1002/2017JD026461, 2017.

Li, Y., Pickering, K. E., Barth, M. C., Bela, M. M., Cummings, K. A., and Allen, D. J.: Evaluation of Parameterized Convective Transport of Trace Gases in Simulation of Storms Observed During the DC3 Field Campaign, Journal of Geophysical Research: Atmospheres, 123, 11,238–11,261, https://doi.org/10.1029/2018JD028779, 2018.

Luo, C., Wang, Y., and Koshak, W. J.: Development of a self-consistent lightning NO x simulation in large-scale 3-D models, Journal of Geophysical Research: Atmospheres, 122, 3141–3154, https://doi.org/10.1002/2016JD026225, 2017.

Marais, E. A., Jacob, D. J., Choi, S., Joiner, J., Belmonte-Rivas, M., Cohen, R. C., Beirle, S., Murray, L. T., Schiferl, L., Shah, V., and Jaeglé, L.: Nitrogen oxides in the global upper troposphere: interpreting cloud-sliced NO<sub>2</sub> observations from the OMI satellite instrument, Atmospheric Chemistry and Physics Discussions, pp. 1–14, https://doi.org/10.5194/acp-2018-556, 2018.

Martin, R. V., Sauvage, B., Folkins, I., Sioris, C. E., Boone, C., Bernath, P., and Ziemke, J.: Space-based constraints on the production of nitric oxide by lightning, Journal of Geophysical Research, 112, 1479, https://doi.org/10.1029/2006JD007831, 2007.

Mecikalski, R. M. and Carey, L. D.: Lightning characteristics relative to radar, altitude and temperature for a multicell, MCS and supercell over northern Alabama, Atmospheric Research, 191, 128–140, https://doi.org/10.1016/j.atmosres.2017.03.001, http://www.sciencedirect.com/science/article/pii/S0169809516302812, 2017.

Min, M., Wu, C., Li, C., Liu, H., Xu, N., Wu, X., Chen, L., Wang, F., Sun, F., Qin, D., Wang, X., Li, B., Zheng, Z., Cao, G., and Dong, L.: Developing the science product algorithm testbed for Chinese next-generation geostationary meteorological satellites: Fengyun-4 series, JOURNAL OF METEOROLOGICAL RESEARCH, 31, 708–719, https://doi.org/10.1007/s13351-017-6161-z, 2017.

Myhre, G., Shindell, D., Bréon, F. M., Collins, W., Fuglestvedt, J., Huang, J., Koch, D., Lamarque, J. F., Lee, D., and Mendoza, B.: Climate change 2013: the physical science basis. Contribution of Working Group I to the Fifth Assessment Report of the Intergovernmental Panel on Climate Change, K., Tignor, M., Allen, SK, Boschung, J., Nauels, A., Xia, Y., Bex, V., and Midgley, PM, Cambridge University Press Cambridge, United Kingdom and New York, NY, USA, 2013.

Nault, B. A., Garland, C., Wooldridge, P. J., Brune, W. H., Campuzano-Jost, P., Crounse, J. D., Day, D. A., Dibb, J., Hall, S. R., Huey, L. G., Jimenez, J. L., Liu, X., Mao, J., Mikoviny, T., Peischl, J., Pollack, I. B., Ren, X., Ryerson, T. B., Scheuer, E., Ullmann, K., Wennberg, P. O., Wisthaler, A., Zhang, L., and Cohen, R. C.: Observational Constraints on the Oxidation of NO x in the Upper Troposphere, The Journal of Physical Chemistry A, 120, 1468–1478, https://doi.org/10.1021/acs.jpca.5b07824, 2016.

Nault, B. A., Laughner, J. L., Wooldridge, P. J., Crounse, J. D., Dibb, J., Diskin, G., Peischl, J., Podolske, J. R., Pollack, I. B., Ryerson, T. B., Scheuer, E., Wennberg, P. O., and Cohen, R. C.: Lightning NO_x Emissions: Reconciling Measured and Modeled Estimates With Updated NO_x Chemistry, Geophysical Research Letters, 44, 9479–9488, https://doi.org/10.1002/2017GL074436, 2017.

Ott, L. E., Pickering, K. E., Stenchikov, G. L., Huntrieser, H., and Schumann, U.: Effects of lightning NO x production during the 21 July European Lightning Nitrogen Oxides Project storm studied with a three-dimensional cloud-scale chemical transport model, Journal of Geophysical Research, 112, 61, https://doi.org/10.1029/2006JD007365, 2007.

Ott, L. E., Pickering, K. E., Stenchikov, G. L., Allen, D. J., DeCaria, A. J., Ridley, B., Lin, R.-F., Lang, S., and Tao, W.-K.: Production of lightning NO_x and its vertical distribution calculated from three-dimensional cloud-scale chemical transport model simulations, Journal of Geophysical Research, 115, 4711, https://doi.org/10.1029/2009JD011880, 2010.

Pickering, K. E., Thompson, A. M., Wang, Y., Tao, W.-K., McNamara, D. P., Kirchhoff, V. W. J. H., Heikes, B. G., Sachse, G. W., Bradshaw, J. D., Gregory, G. L., and Blake, D. R.: Convective transport of biomass burning emissions over Brazil during TRACE A, Journal of Geophysical Research, 101, 23 993–24 012, https://doi.org/10.1029/96JD00346, 1996.

Pickering, K. E., Bucsela, E., Allen, D., Ring, A., Holzworth, R., and Krotkov, N.: Estimates of lightning NO_x production based on OMI NO_2 observations over the Gulf of Mexico, Journal of Geophysical Research: Atmospheres, 121, 8668–8691, https://doi.org/10.1002/2015JD024179, 2016.

Platt, U. and Perner, D.: Measurements of Atmospheric Trace Gases by Long Path Differential UV/Visible Absorption Spectroscopy, in: Optical and Laser Remote Sensing, edited by Schawlow, A. L., Killinger, D. K., and Mooradian, A., vol. 39 of *Springer Series in Optical Sciences*, pp. 97–105, Springer Berlin Heidelberg, Berlin, Heidelberg, https://doi.org/10.1007/978-3-540-39552-2_13, 1983.

695 Price, C. and Rind, D.: A simple lightning parameterization for calculating global lightning distributions, Journal of Geophysical Research, 97, 9919–9933, https://doi.org/10.1029/92JD00719, 1992.

Richter, A., Burrows, J. P., Nüß, H., Granier, C., and Niemeier, U.: Increase in tropospheric nitrogen dioxide over China observed from space, Nature, 437, 129–132, https://doi.org/10.1038/nature04092, 2005.

Romps, D. M.: Evaluating the future of lightning in cloud-resolving models, Geophysical Research Letters, 700 https://doi.org/10.1029/2019GL085748, 2019.

Romps, D. M., Seeley, J. T., Vollaro, and Molinari, J.: Projected increase in lightning strikes in the United States due to global warming, Atmospheric Chemistry and Physics, 346, 851–854, https://doi.org/10.1126/science.1259100, 2014.

Rudlosky, S.: Evaluating ENTLN performance relative to TRMM/LIS, Journal of Operational Meteorology, 3, 11–20, https://doi.org/10.15191/nwajom.2015.0302, 2015.

705 Schaaf, C. B., Liu, J., Gao, F., and Strahler, A. H.: Aqua and Terra MODIS Albedo and Reflectance Anisotropy Products, in: Land Remote Sensing and Global Environmental Change, edited by Ramachandran, B., Justice, C. O., and Abrams, M. J., vol. 11 of *Remote Sensing and Digital Image Processing*, pp. 549–561, Springer New York, New York, NY, https://doi.org/10.1007/978-1-4419-6749-7_24, 2011.

Schumann, U. and Huntrieser, H.: The global lightning-induced nitrogen oxides source, Atmospheric Chemistry and Physics, 7, 3823–3907, https://doi.org/10.5194/acp-7-3823-2007, 2007.

710 Schwantes, R. H., Teng, A. P., Nguyen, T. B., Coggon, M. M., Crounse, J. D., St Clair, J. M., Zhang, X., Schilling, K. A., Seinfeld, J. H., and Wennberg, P. O.: Isoprene NO3 Oxidation Products from the RO2 + HO2 Pathway, The Journal of Physical Chemistry A, 119, 10 158–10 171, https://doi.org/10.1021/acs.jpca.5b06355, 2015.

Silvern, R. F., Jacob, D. J., Travis, K. R., Sherwen, T., Evans, M. J., Cohen, R. C., Laughner, J. L., Hall, S. R., Ullmann, K., Crounse, J. D., Wennberg, P. O., Peischl, J., and Pollack, I. B.: Observed NO/NO_2 ratios in the upper troposphere imply errors in $NO-NO_2-O_3$ cycling 715 kinetics or an unaccounted NO_x reservoir, Geophysical Research Letters, https://doi.org/10.1029/2018GL077728, 2018.

Sneep, M., de Haan, J. F., Stammes, P., Wang, P., Vanbauce, C., Joiner, J., Vasilkov, A. P., and Levelt, P. F.: Three-way comparison between OMI and PARASOL cloud pressure products, Journal of Geophysical Research, 113, D05 204, https://doi.org/10.1029/2007JD008694, 2008.

Stammes, P., Sneep, M., de Haan, J. F., Veefkind, J. P., Wang, P., and Levelt, P. F.: Effective cloud fractions from the Ozone Monitoring Instrument: Theoretical framework and validation, Journal of Geophysical Research, 113, D05 204, https://doi.org/10.1029/2007JD008820, 720 2008.

Strode, S. A., Douglass, A. R., Ziemke, J. R., Manyin, M., Nielsen, J. E., and Oman, L. D.: A Model and Satellite-Based Analysis of the Tropospheric Ozone Distribution in Clear Versus Convectively Cloudy Conditions, Journal of Geophysical Research: Atmospheres, 122, 11,948–11,960, https://doi.org/10.1002/2017JD027015, 2017.

725 Travis, K. R., Jacob, D. J., Fisher, J. A., Kim, P. S., Marais, E. A., Zhu, L., Yu, K., Miller, C. C., Yantosca, R. M., Sulprizio, M. P., Thompson, A. M., Wennberg, P. O., Crounse, J. D., St Clair, J. M., Cohen, R. C., Laughner, J. L., Dibb, J. E., Hall, S. R., Ullmann, K., Wolfe, G. M., Pollack, I. B., Peischl, J., Neuman, J. A., and Zhou, X.: Why do Models Overestimate Surface Ozone in the Southeastern United States?, Atmospheric Chemistry and Physics, 16, 13 561–13 577, https://doi.org/10.5194/acp-16-13561-2016, 2016.

Vasilkov, A., Joiner, J., Spurr, R., Bhartia, P. K., Levelt, P., and Stephens, G.: Evaluation of the OMI cloud pressures derived from rotational Raman scattering by comparisons with other satellite data and radiative transfer simulations, Journal of Geophysical Research, 113, D05 204, https://doi.org/10.1029/2007JD008689, 2008.

Veefkind, J. P., Aben, I., McMullan, K., Förster, H., de Vries, J., Otter, G., Claas, J., Eskes, H. J., de Haan, J. F., Kleipool, Q., van Weele, M., Hasekamp, O., Hoogeveen, R., Landgraf, J., Snel, R., Tol, P., Ingmann, P., Voors, R., Kruizinga, B., Vink, R., Visser, H., and Levelt, P. F.: TROPOMI on the ESA Sentinel-5 Precursor: A GMES mission for global observations of the atmospheric composition for climate, air quality and ozone layer applications, Remote Sensing of Environment, 120, 70–83, https://doi.org/10.1016/j.rse.2011.09.027, 2012.

Wang, L., Follette-Cook, M. B., Newchurch, M. J., Pickering, K. E., Pour-Biazar, A., Kuang, S., Koshak, W., and Peterson, H.: Evaluation of lightning-induced tropospheric ozone enhancements observed by ozone lidar and simulated by WRF/Chem, Atmospheric Environment, 115, 185–191, https://doi.org/10.1016/j.atmosenv.2015.05.054, 2015.

Williams, E. R.: The tripole structure of thunderstorms, Journal of Geophysical Research, 94, 13 151, https://doi.org/10.1029/JD094iD11p13151, 1989.

Wong, J., Barth, M. C., and Noone, D.: Evaluating a lightning parameterization based on cloud-top height for mesoscale numerical model simulations, Geoscientific Model Development, 6, 429–443, https://doi.org/10.5194/gmd-6-429-2013, 2013.

Xu, K.-M. and Randall, D. A.: A Semiempirical Cloudiness Parameterization for Use in Climate Models, Journal of the Atmospheric Sciences, 53, 3084–3102, https://doi.org/10.1175/1520-0469(1996)053<3084:ASCPFU>2.0.CO;2, 1996.

Yang, J., Zhang, Z., Wei, C., Lu, F., and Guo, Q.: Introducing the New Generation of Chinese Geostationary Weather Satellites, Fengyun-4, Bulletin of the American Meteorological Society, 98, 1637–1658, https://doi.org/10.1175/BAMS-D-16-0065.1, 2017.

Zel'dovich, Y. and Raizer, Y.: VIII - Physical and chemical kinetics in hydrodynamic processes, in: Physics of Shock Waves and High-Temperature Hydrodynamic Phenomena, edited by Hayes, W. D., Probstein, R. F., Zel'dovich, Y., and Raizer, Y., pp. 566–571, Academic Press, https://doi.org/10.1016/B978-0-12-395672-9.50009-6, 1967.

Zhang, P., Lu, Q., Hu, X., Gu, S., Yang, L., Min, M., Chen, L., Xu, N., Sun, L., Bai, W., Ma, G., and Di Xian: Latest Progress of the Chinese Meteorological Satellite Program and Core Data Processing Technologies, Advances in Atmospheric Sciences, 36, 1027–1045, https://doi.org/10.1007/s00376-019-8215-x, 2019.

Zhang, X. and Laughner, J.: zxdawn/BEHR-LNOx: v1.0, Zenodo, https://doi.org/10.5281/zenodo.3553426, 2019.

Zhao, C., Wang, Y., Choi, Y., and Zeng, T.: Summertime impact of convective transport and lightning NO_x production over North America: modeling dependence on meteorological simulations, Atmospheric Chemistry and Physics, 9, 4315–4327, https://doi.org/10.5194/acp-9-4315-2009, 2009.

Zhou, Y., Brunner, D., Boersma, K. F., Dirksen, R., and Wang, P.: An improved tropospheric NO_2 retrieval for OMI observations in the vicinity of mountainous terrain, Atmospheric Measurement Techniques, 2, 401–416, https://doi.org/10.5194/amt-2-401-2009, 2009.

Zhu, Q., Laughner, J. L., and Cohen, R. C.: Lightning NO 2 simulation over the contiguous US and its effects on satellite NO 2 retrievals, Atmospheric Chemistry and Physics, 19, 13 067–13 078, https://doi.org/10.5194/acp-19-13067-2019, 2019.

Zhu, Y., Rakov, V. A., Tran, M. D., and Nag, A.: A study of National Lightning Detection Network responses to natural lightning based on ground truth data acquired at LOG with emphasis on cloud discharge activity, Journal of Geophysical Research: Atmospheres, 121, 14,651–14,660, https://doi.org/10.1002/2016JD025574, 2016.

Zhu, Y., Rakov, V. A., Tran, M. D., Stock, M. G., Heckman, S., Liu, C., Sloop, C. D., Jordan, D. M., Uman, M. A., Caicedo, J. A., Kotovsky, D. A., Wilkes, R. A., Carvalho, F. L., Ngin, T., Gamerota, W. R., Pilkey, J. T., and Hare, B. M.: Evaluation of ENTLN Performance

Characteristics Based on the Ground Truth Natural and Rocket-Triggered Lightning Data Acquired in Florida, Journal of Geophysical Research: Atmospheres, 122, 9858–9866, https://doi.org/10.1002/2017JD027270, 2017.

Ziemke, J. R., Joiner, J., Chandra, S., Bhartia, P. K., Vasilkov, A., Haffner, D. P., Yang, K., Schoeberl, M. R., Froidevaux, L., and Levelt, P. F.: Ozone mixing ratios inside tropical deep convective clouds from OMI satellite measurements, Atmospheric Chemistry and Physics, 9, 573–583, https://doi.org/10.5194/acp-9-573-2009, 2009.

Ziemke, J. R., Strode, S. A., Douglass, A. R., Joiner, J., Vasilkov, A., Oman, L. D., Liu, J., Strahan, S. E., Bhartia, P. K., and Haffner, D. P.: A cloud-ozone data product from Aura OMI and MLS satellite measurements, Atmospheric Measurement Techniques, 10, 4067–4078, https://doi.org/10.5194/amt-10-4067-2017, 2017.

770
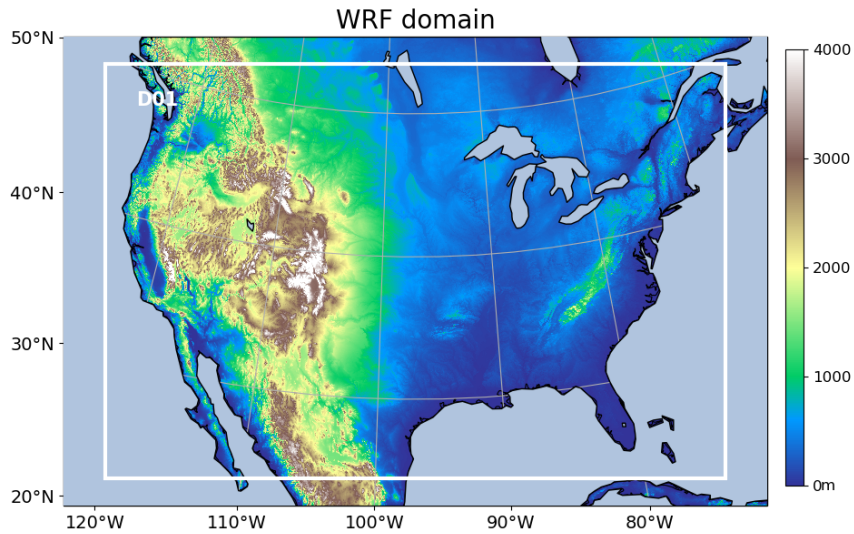
Figure 1. Domain and terrain height (m) of the WRF-Chem simulation with 350 x 290 grid cells and a horizontal resolution of 12 km.
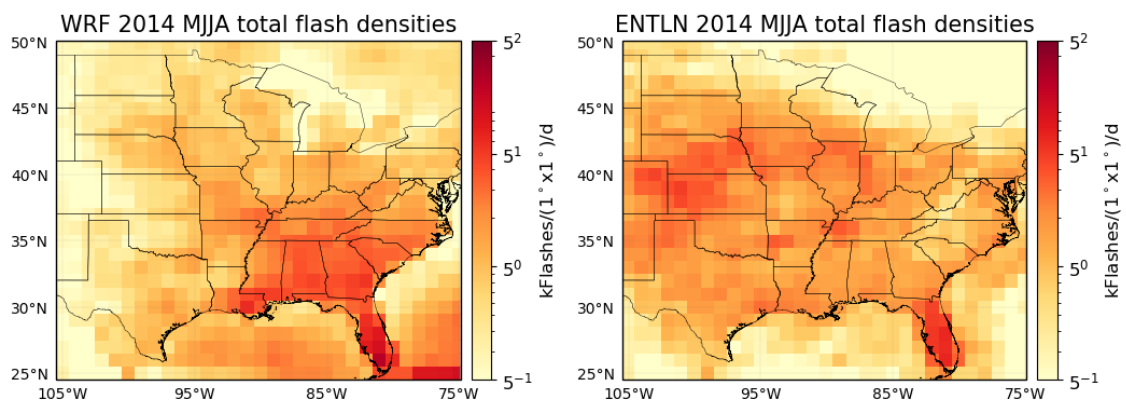
Figure 2. Comparison between total flash densities from ENTLN and WRF-Chem during MJJA 2014.

Table 1. Definitions of the abbreviations for the criteria used in this study.

Abbreviations	Full form [source]
CRF	Cloud radiance fraction [OMI]
CP	Cloud optical pressure [OMI]
CF	Cloud fraction [WRF-Chem]
TL	Total lightning flashes [WRF-Chem]
ratio	modeled LNO_2 Vis / modeled NO_2 Vis [WRF-Chem]
CRFα_ENTLN	CRF $\geq \alpha$ + ENTLN flashes(strokes) $\geq$ 2400(8160) [ENTLN]
CRFα_CF40_ENTLN	CRF $\geq \alpha$ + ENTLN flashes(strokes) $\geq$ 2400(8160) + CF $\geq$ 40%
CRFα_ENTLN_TL1000	CRF $\geq \alpha$ + ENTLN flashes(strokes) $\geq$ 2400(8160) + TL $\geq$ 1000
CRFα_CF40_ENTLN_TL1000	CRF $\geq \alpha$ + ENTLN flashes(strokes) $\geq$ 2400(8160) + CF $\geq$ 40% + TL $\geq$ 1000
CRFα_ENTLN_TL1000_ratio50	CRF $\geq \alpha$ + ENTLN flashes(strokes) $\geq$ 2400(8160) + TL $\geq$ 1000 + ratio $\geq$ 50%
CRFα_CF40_ENTLN_TL1000_ratio50	CRF $\geq \alpha$ + ENTLN flashes(strokes) $\geq$ 2400(8160) + CF $\geq$ 40% + TL $\geq$ 1000 + ratio $\geq$ 50%

α has three options: 70%, 90% and 100%

Table 2. LNO_x production for different combinations of criteria defined in Table 1.

Condition[1]	ENTLN data type[2]	LNO$_x$/flash or LNO$_x$/stroke	R value	Intercept (10^6 mol)	Days[3]
CRF90_ENTLN	Flash	52.1 ± 51.1	0.20	0.21	99
CRF90_CF40_ENTLN	Flash	84.2 ± 31.5	0.54	-0.04	70
CRF90_ENTLN_TL1000	Flash	61.9 ± 49.1	0.27	0.33	83
CRF90_CF40_ENTLN_TL1000	Flash	63.4 ± 52.9	0.38	0.26	38
CRF90_ENTLN_TL1000_ratio50	Flash	54.5 ± 48.1	0.25	0.39	81
CRF90_CF40_ENTLN_TL1000_ratio50	Flash	90.0 ± 65.0	0.46	0.15	32
CRF90_ENTLN	Stroke	6.7 ± 4.1	0.31	0.23	102
CRF90_CF40_ENTLN	Stroke	10.3 ± 3.6	0.55	0.08	79
CRF90_ENTLN_TL1000	Stroke	7.5 ± 5.1	0.29	0.38	94
CRF90_CF40_ENTLN_TL1000	Stroke	8.6 ± 6.2	0.39	0.27	46
CRF90_ENTLN_TL1000_ratio50	Stroke	7.0 ± 4.8	0.29	0.42	93
CRF90_CF40_ENTLN_TL1000_ratio50	Stroke	8.9 ± 7.0	0.39	0.31	40

[1] These conditions are defined in Table 1. [2] The threshold of ENTLN data is 2400 flashes box^{-1} and 8160 strokes box^{-1} during the period of 2.4 h before OMI overpass time. [3] The number of valid days with specific criteria in MJJA 2014.

Table 3. LNO_x production for different thresholds of CRF with coincident ENTLN data, TL $\geq$ 1000 and ratio $\geq$ 50%.

CRF (%)	ENTLN data type[1]	LNO_x/flash or LNO_x/stroke	R value	Intercept (10^5 mol)	Days[2]
70	Flash	35.7 ± 36.8	0.21	4.91	85
90	Flash	54.5 ± 48.1	0.25	3.90	81
100	Flash	20.8 ± 37.4	0.13	5.67	71
70	Stroke	4.1 ± 3.9	0.21	5.16	96
90	Stroke	7.0 ± 4.8	0.29	4.16	93
100	Stroke	2.6 ± 4.0	0.14	5.41	82

[1] The threshold of ENTLN data is 2400 flashes box^{-1} and 8160 strokes box^{-1} during the period of 2.4 h before OMI overpass time. [2] The number of valid days with specific criteria in MJJA 2014.
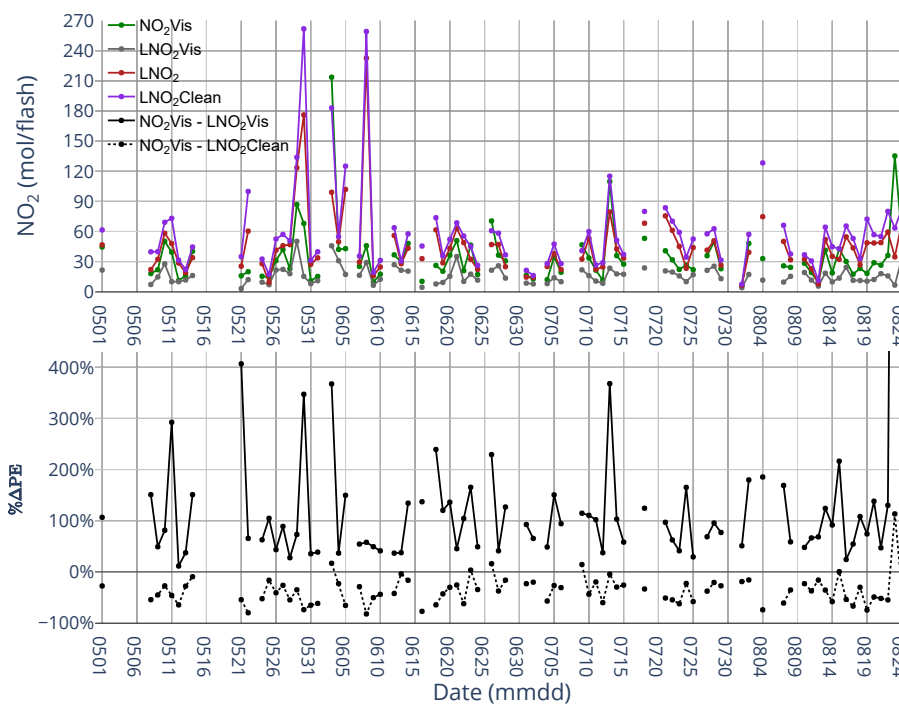
Figure 3. (top) Time series of NO_2Vis, LNO_2Vis, LNO_2 and LNO_2Clean production per day over the CONUS for MJJA 2014 with CRF $\geq$ 90% and a flash threshold of 2400 flashes per 2.4 h. (bottom) Time series of the percent differences between NO_2Vis and LNO_2Vis and the percent differences between NO_2Vis and LNO_2Clean with CRF $\geq$ 90%. The value of black dot on August 23 (not shown) is 1958%.
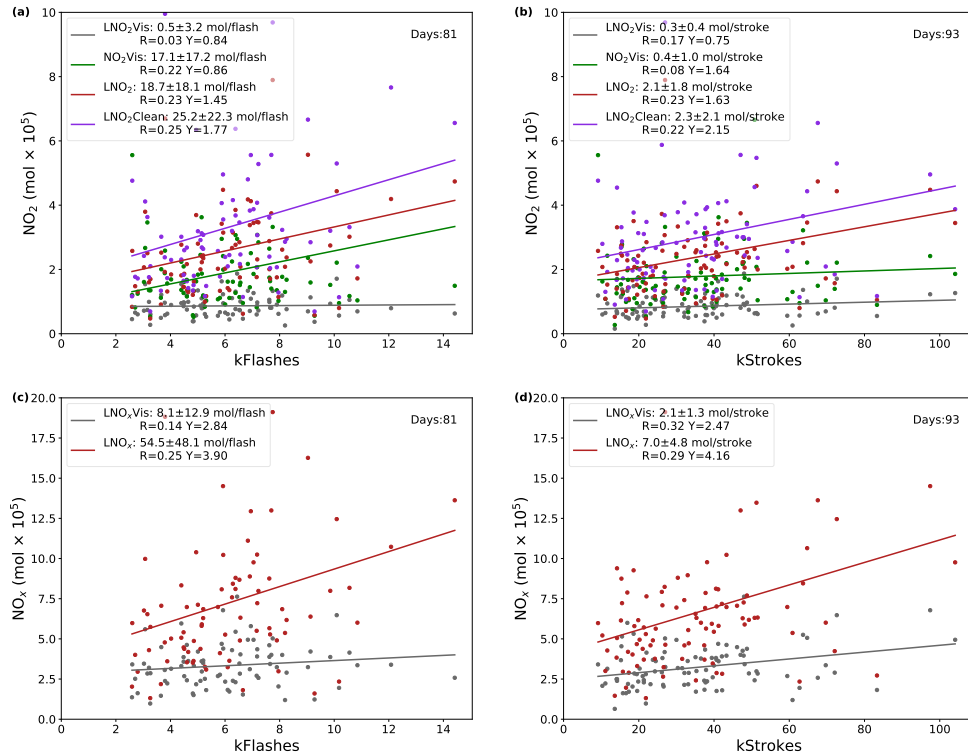
Figure 4. (a) Daily NO_2Vis, LNO_2Vis, LNO_2 and LNO_2Clean versus ENTLN total flashes data. (b) Same as (a) but for strokes. (c) Daily LNO_xVis and LNO_x versus total flashes. (d) Same as (c) but for strokes.

Table 4. The percent change in the estimated production when using different methods based on the same a priori profiles.

	City[1]	(LNO_2Clean - LNO_2)/LNO_2	(LNO_2 - TropVis)/TropVis	(LNO_2Clean-TropVis)/TropVis
Polluted	Lansing	24.2%	49.5%	85.6%
	New Orleans	13.3%	121.2%	153.8%
	Orlando	46.3%	37.5%	101.3%
Clean	Huron	12.0%	56.4%	75.2%
	Charles Town	12.0%	82.2%	104.1%
	Tarboro	5.0%	86.0%	95.3%

[1]Locations are denoted in Fig. 6a.
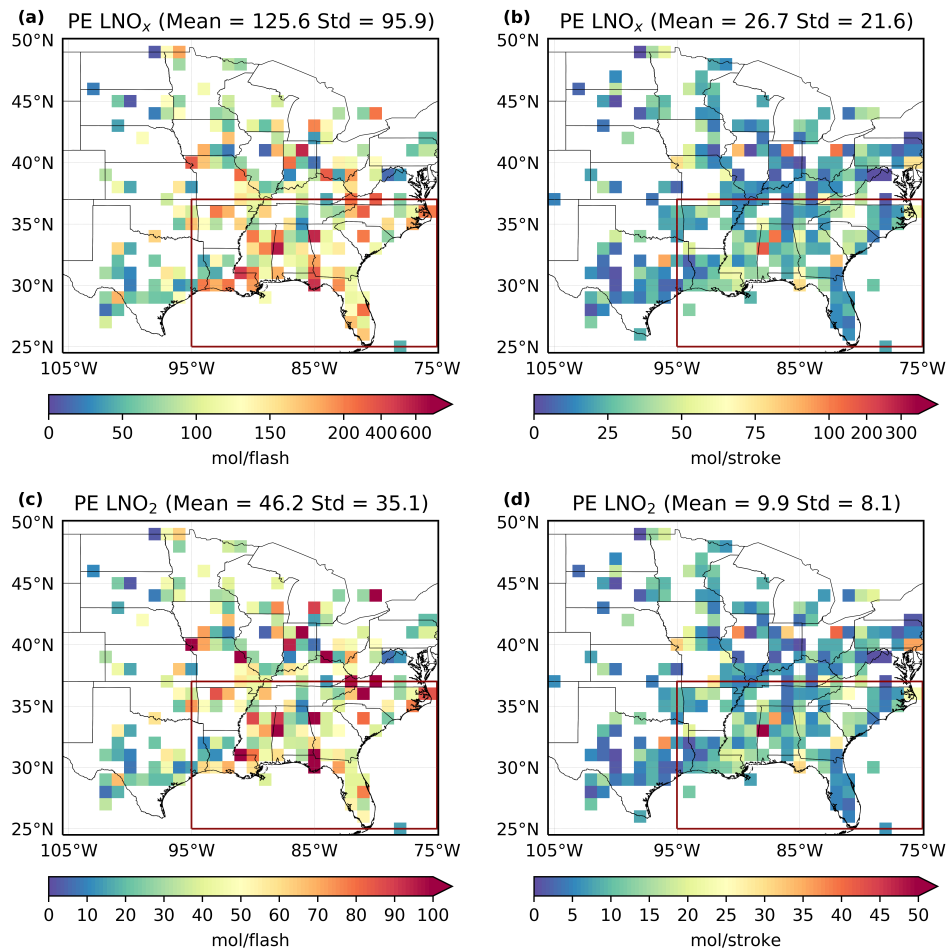
Figure 5. (a) and (c) Maps of $1° \times 1°$ gridded values of mean LNO_x and LNO_2 production per flash with CRF $\geq 90\%$ for MJJA 2014. (b) and (d) Same as (a) and (c) except for strokes. The southeastern US is denoted by the red box in panels a – d.
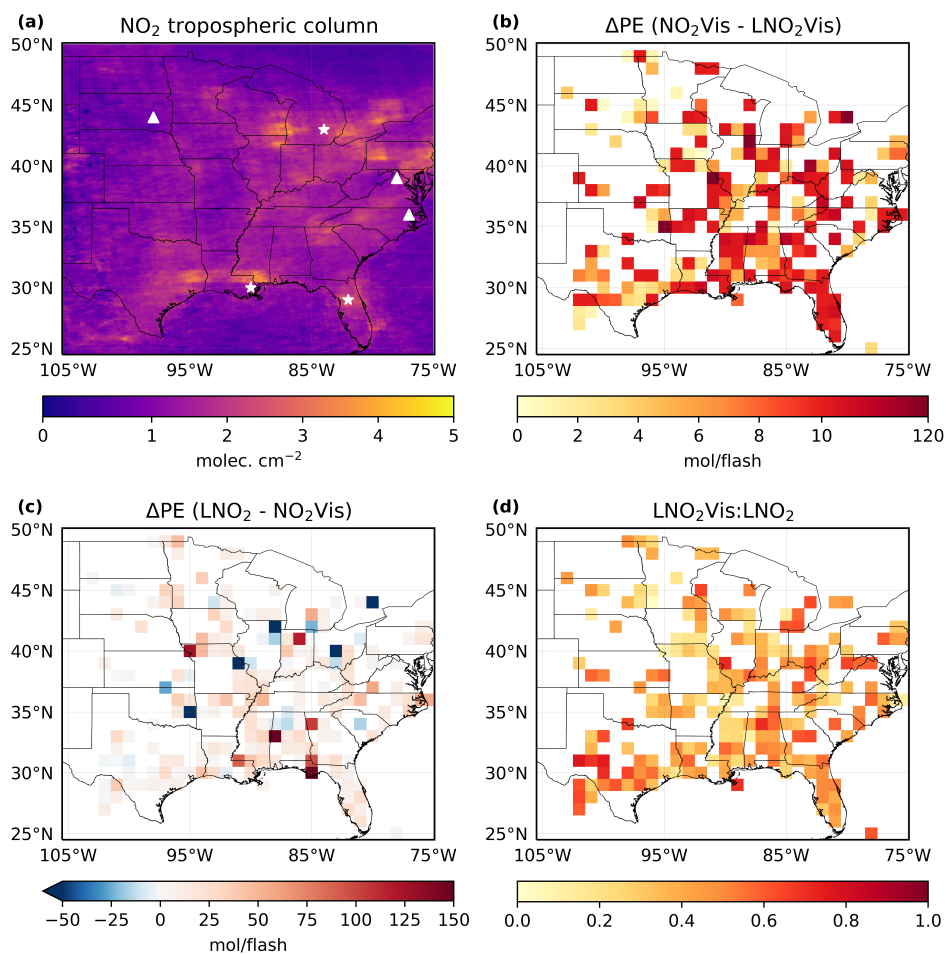
Figure 6. (a) Mean (MJJA 2014) NO_2 tropospheric column. Polluted cities are denoted by stars: Lansing, New Orleans and Orlando while clean cities are denoted by triangles: Huron, Charles Town and Tarboro. (b) The differences of the estimated mean production efficiency between NO_2Vis and LNO_2Vis with CRF $\geq$ 90%. (c) The same differences as (b) but between LNO_2 and NO_2Vis. (d) The ratio of LNO_2Vis to LNO_2.
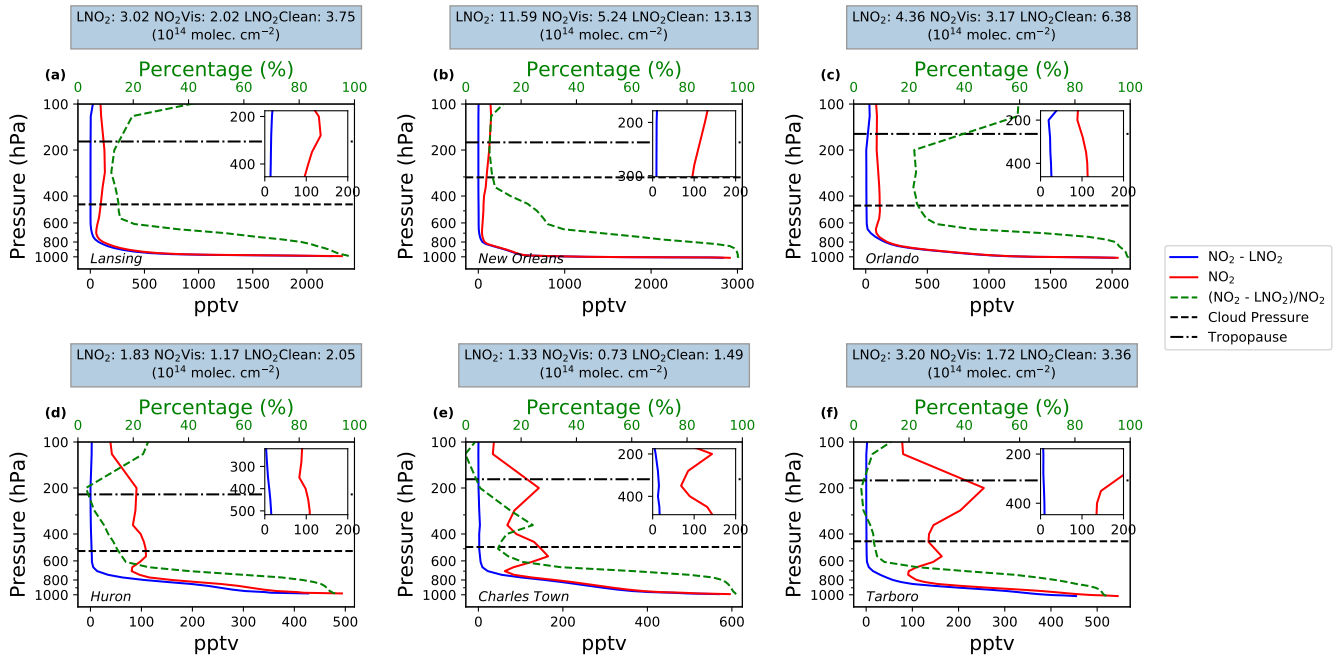
Figure 7. Comparison of mean WRF-Chem NO_2 and background NO_2 profiles in six grids with CRF ≥ 100% on specific days during MJJA 2014. The top row data are selected from polluted regions (stars in Fig. 6a) while the bottom row data are from clean regions (triangles in Fig. 6a). The green dashed lines are the mean ratio profiles of background NO_2 to NO_2. The zoomed figures show the profiles from the cloud pressure to the tropopause. The titles present the mean productions based on three different methods mentioned in Sect. 2.4.
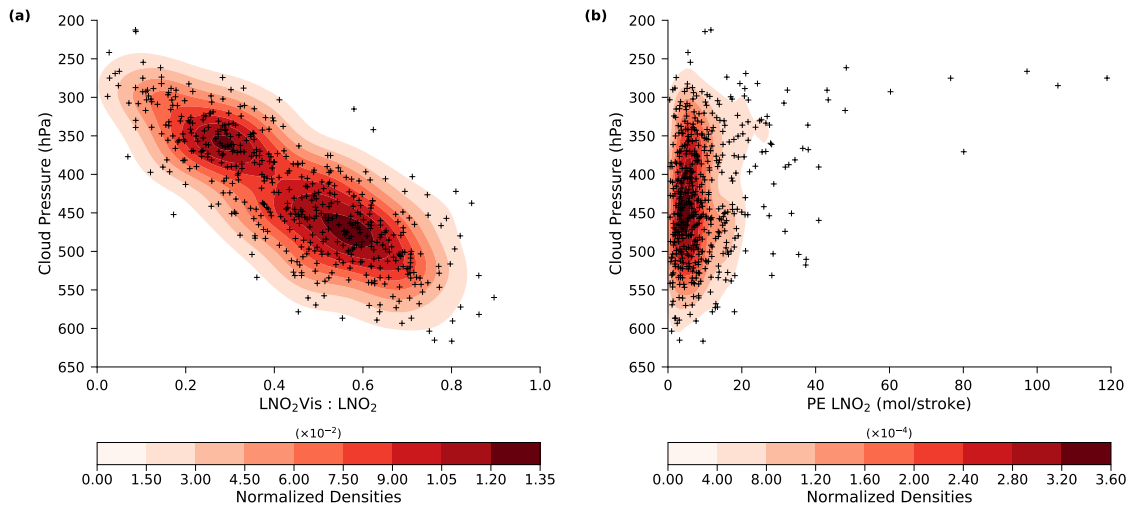
Figure 8. Kernel density estimation of the (a) daily ratio of LNO_2Vis to LNO_2 and (b) daily LNO_2 production efficiency versus the daily cloud pressure measured by OMI with CRF ≥ 90% for MJJA 2014.
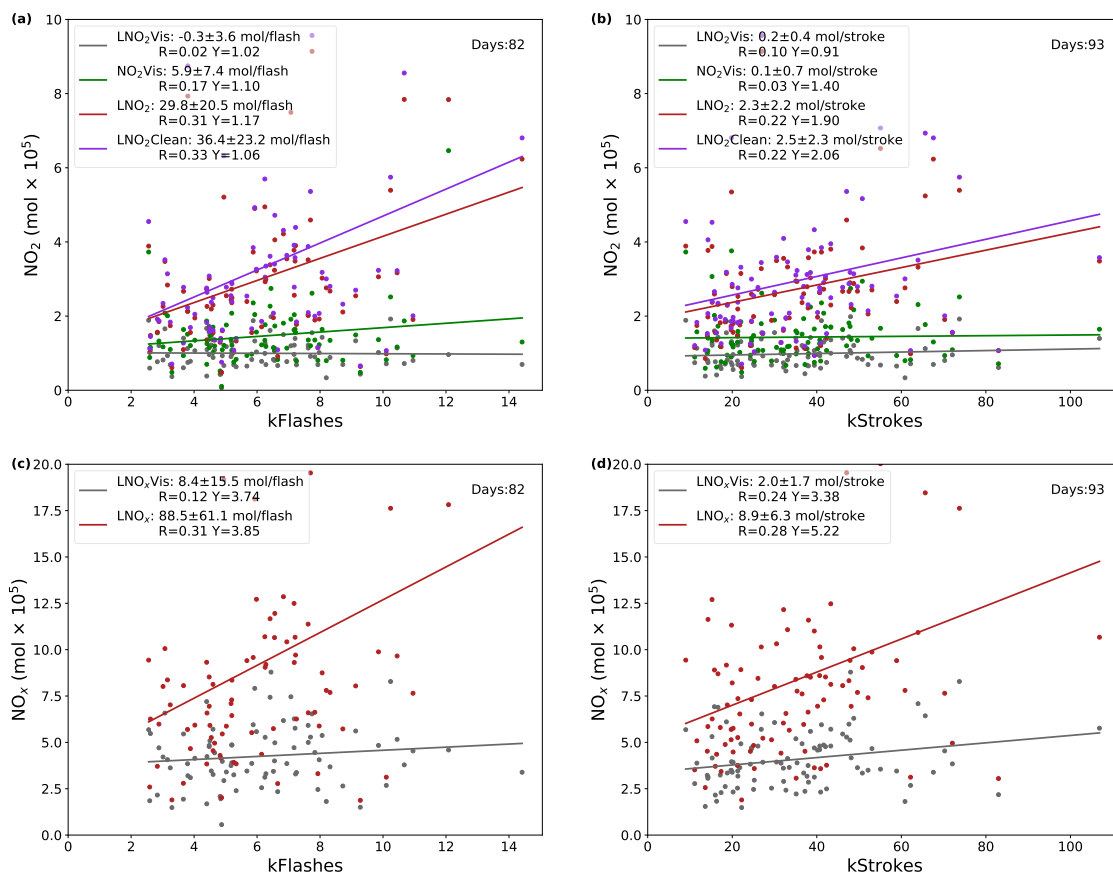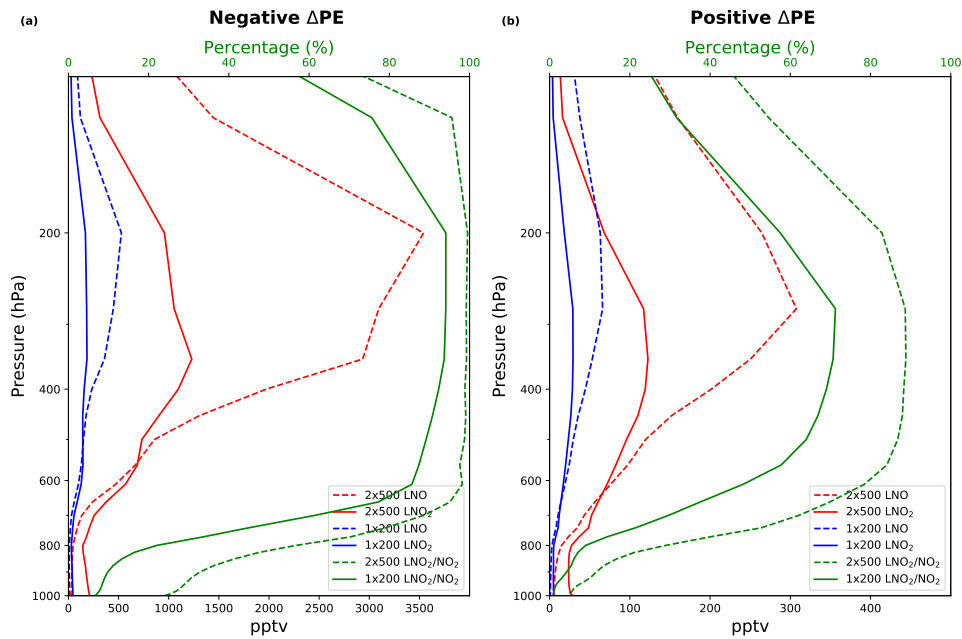
Figure 9. Same as Fig. 4 except for 2×500 mol NO flash^{-1} configuration.
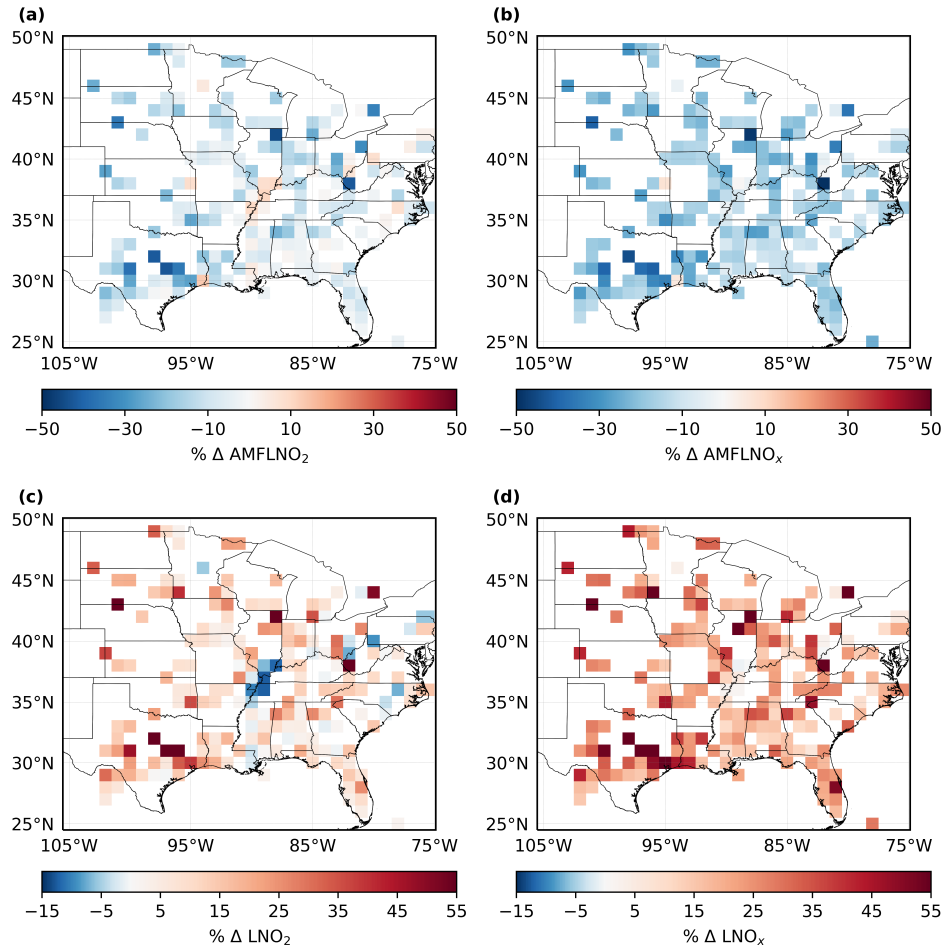
Figure 10. Average percent difference in (a) AMF_{LNO_2}, (b) AMF_{LNO_x}, (c) LNO_2 and (d) LNO_x with $CRF \geq 90\%$ over MJJA 2014. Difference between profiles are generated by 2×500 mol NO flash^{-1} and 1×200 mol NO flash^{-1}.

Figure 11. LNO and LNO_2 profiles with different LNO settings at (a) the region containing the minimal negative percent change in LNO_2 and (b) the region containing the largest positive percent change in LNO_2 when the LNO setting is changed from 1×200 mol NO flash^{-1} to 2×500 mol NO flash^{-1}, averaged over MJJA 2014. The profiles using 1×200 (2×500) mol NO flash^{-1} are shown in blue (red) lines. Solid (dashed) green lines are the mean ratio of LNO_2 to NO_2 with 1×200 (2×500) mol NO flash^{-1}.
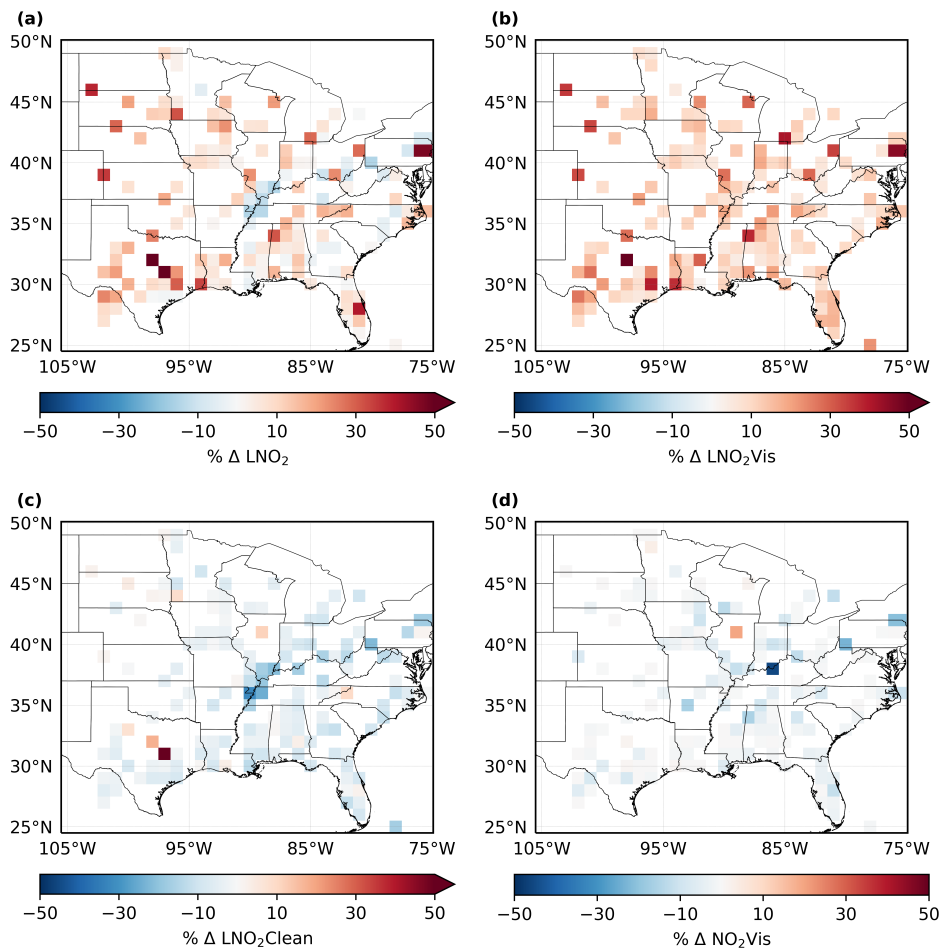
Figure 12. Average percent difference in (a) LNO$_2$, (b) LNO$_2$Vis, (c) LNO$_2$Clean and (d) NO$_2$Vis with CRF = 100% over MJJA 2014.

Table 5. Uncertainties for the estimation of LNO_2/flash, LNO_x/flash, LNO_2/stroke and LNO_x/stroke.

Type	Perturbation	LNO_2/flash[5]	LNO_x/flash[5]	LNO_2/stroke[5]	LNO_x/stroke[5]
BEHR tropopause pressure[1]	NASA product tropopause	6	4	6	4
Cloud radiance fraction[1]	$\pm$ 5%	2	2	2	2
Cloud pressure[2]	Constant AMF: 0.46	23	23	23	23
Surface pressure[1]	$\pm$ 1.5%	0	0	0	0
Surface reflectivity[1]	$\pm$ 17%	0	0	0	0
LNO_2 profile[1]	2×500 mol NO flash^{-1}	15	29	14	29
Profile location[1]	Quasi-Monte Carlo	0	1	0	1
Lightning detection efficiency[3]	IC: $\pm$ 16%, CG: $\pm$ 5%	15	15	15	15
t_{window}[3]	2 – 4 hours	10	10	8	8
LNO_x lifetime[3]	2 – 12 hours	24	24	24	24
V_{strat}[4]	-	10	10	10	10
Systematic errors in slant column[4]	-	5	5	5	5
Tropospheric background[4]	-	10	10	10	10
NO/NO_2[4]	-	20	20	20	20
Net	-	48	54	47	54

$PE_{uncertainty}$ = (Error$_{rising\ perturbed\ value}$ - Error$_{lowering\ perturbed\ value}$)/2 where Error$_{perturbed\ value}$ = ($PE_{perturbed\ value}$ - $PE_{original\ value}$)/$PE_{original\ value}$.
[1] Laughner et al. (2019) [2] Beirle et al. (2009) [3] Lapierre et al. (2019) [4] Allen et al. (2019) and Bucsela et al. (2019) [5] Uncertainty (%)

Table A1. Simple forms of abbreviations for AMFs.

Abbreviations	Numerator[1]	Denominator[2]
AMF_{LNO_2}	S_{NO_2}	V_{LNO_2}
$AMF_{LNO_2\,Vis}$	S_{NO_2}	$V_{LNO_2\,Vis}$
$AMF_{LNO_2\,Clean}$	S_{LNO_2}	V_{LNO_2}
$AMF_{NO_2\,Vis}$	S_{NO_2}	$V_{NO_2\,Vis}$
AMF_{LNO_x}	S_{NO_2}	V_{LNO_x}
$AMF_{NO_x\,Vis}$	S_{NO_2}	$V_{NO_x\,Vis}$

[1] The part of simulated VCD seen by OMI [2] The simulated VCD